

Study of the pion-mass dependence of ρ -meson properties in lattice QCD

Kang Yu,¹ Yan Li,² Jia-Jun Wu,^{1,3} Derek B. Leinweber,⁴ and Anthony W. Thomas⁴

¹*School of Physical Sciences, University of Chinese Academy of Sciences, Beijing 100049, China*

²*Department of Physics, University of Cyprus, 20537 Nicosia, Cyprus*

³*Southern Center for Nuclear-Science Theory (SCNT), Institute of Modern Physics, Chinese Academy of Sciences, Huizhou 516000, Guangdong Province, China*

⁴*Special Research Centre for the Subatomic Structure of Matter (CSSM), Department of Physics, University of Adelaide, Adelaide, South Australia 5005, Australia*

(Dated: March 18, 2024)

We collect spectra extracted in the $I = \ell = 1$ $\pi\pi$ sector provided by various lattice QCD collaborations and study the m_π dependence of ρ -meson properties using Hamiltonian Effective Field Theory (HEFT). In this unified analysis, the coupling constant and cutoff mass, characterizing the $\rho - \pi\pi$ vertex, are both found to be weakly dependent on m_π , while the mass of the bare ρ , associated with a simple quark-model state, shows a linear dependence on m_π^2 . Both the lattice results and experimental data can be described well. Drawing on HEFT's ability to describe the pion mass dependence of resonances in a single formalism, we map the dependence of the phase shift as a function of m_π , and expose interesting discrepancies in contemporary lattice QCD results.

I. INTRODUCTION

One of the most significant challenges in hadron physics is to understand the internal composition of diverse hadrons. However, because of the non-perturbative nature of the strong interaction in the low energy regime, the structure of hadrons within Quantum Chromodynamics (QCD) has remained unsolvable analytically. In order to develop insight into hadron structure and guide experimental work, a wide variety of phenomenological models have been developed. This includes the constituent quark model [1], the MIT [2] and cloudy bag models [3, 4] as well others based upon Schwinger-Dyson equations [5] and molecular [6] and hybrid [7] models. As it is often possible to adjust the parameters in these models in order to reproduce the limited experimental data, these models can typically not be distinguished solely on the basis of how well they describe experiments.

On the other hand, the approximate chiral symmetry of QCD means that the pion is a pseudo-Goldstone boson, with a much smaller mass, m_π , than other hadrons. Because the mass of the pion squared is proportional to the quark mass over a wide range, it is reasonable to expand certain physical variables in terms of m_π . For instance, the mass of a resonance R can be expressed perturbatively as follows:

$$m_R = \sum_{n=0}^{\infty} \alpha_n(\{g_i\}) m_\pi^{2n} + \Sigma_R(\{g_i\}, m_\pi), \quad (1)$$

where $\{g_i\}$ is the set of free parameters of the model and Σ_R is the self-energy term. The separation described in Eq. 1 differentiates between the known model-independent coefficients of terms nonanalytic in the quark mass which are contained within the self-energy terms, and the unknown coefficients of terms analytic in the quark mass, coefficients that are constrained by fitting data.

In the real world, m_π takes the fixed value $\mu_\pi \approx 138.5$

MeV (for charged pions), and it is typically feasible to adjust the free parameters of a model, $\{g_i\}$, to reproduce the correct experimental value, $m_R(\mu_\pi)$. However, when we extend the model to unphysical pion masses these models may predict different values of m_R versus m_π . The dependence of various physical variables on m_π offers a fresh perspective in exploring the structure of hadrons in the non-perturbative regime [8]. As a result, it is of great significance to make measurements on m_R at unphysical m_π values.

Lattice QCD (LQCD) is a well-established non-perturbative formulation of QCD, defined on a finite and discretized volume of four-dimensional Euclidean spacetime. Through simulation of the two-point Green functions of composite operators, one can obtain the finite volume spectrum of eigenvalues of the QCD Hamiltonian, with specific quantum numbers, as a function of m_π . We stress that such results are genuine predictions of QCD, even though the light quark masses do not take their physical values. Moreover, the phase shift in the infinite volume can then be obtained through the well-known Lüscher formula and its extensions [9–14].

LQCD has developed rapidly over the half century since Wilson's pioneering work was published in 1974 [15]. With the substantial progress in simulation algorithms and tremendous advances in computing power, many LQCD collaborations [16, 17] have extracted the finite volume spectra for various sets of quantum numbers, including the ρ meson, over a range of values of m_π .

Experimentally, the ρ meson is identified as a broad peak around $\sqrt{s} = 770$ MeV in the invariant mass distribution of the isovector P -wave of $\pi\pi$ scattering [18]. It is often identified as a confined $q\bar{q}$ state, consistent with the constituent quark model. This picture is supported by several theoretical arguments, such as the the large- N_c limit of QCD [19–22]. Nevertheless, the sizable decay width, $\Gamma_{\rho \rightarrow \pi\pi} \approx 140$ MeV [18], signifies the ρ meson's strong coupling to the $\pi\pi$ channel. In other words, the observed peak structure results from the interaction be-

tween a $q\bar{q}$ state, referred to as the bare ρ , and the $\pi\pi$ continuum at the hadronic level. Consequently, a comprehensive study of the ρ meson necessitates an exploration of the $\pi\pi$ scattering sector.

In the past decade, multiple LQCD groups have provided energy levels for the P -wave $\pi\pi$ sector [23–36]. However, there has been little work collating spectra from various collaborations [37, 38], particularly for $N_f = 2 + 1$, and performing a consistent unified analysis. That is the aim of this paper.

The Lüscher formula is the most practical way to relate lattice calculations to the elastic scattering phase shifts of two spinless particles. Therefore, when dealing with a system containing only one $\pi\pi$ channel, it is sufficient to utilize the standard Lüscher formula to relate the finite volume spectrum to the phase shifts. However, in our present study, we also aim to incorporate the $\omega\pi$ channel, in order to assess its impact. While it is not an open channel, it does generate the leading non-analytic behaviour of the ρ mass as a function of m_π .

While the Lüscher formalism can certainly include the additional $\omega\pi$ channel, we note that there are other approaches which provide computational convenience with very little overhead in incorporating several two-particle channels. As an example, we mention that the unitarized chiral perturbation theory (χ Pt) can calculate the finite volume spectrum through the pole position of the T matrix defined in the finite volume as shown in Refs. [39, 40].

Alternatively, Hamiltonian effective field theory (HEFT) also incorporates the Lüscher formalism and establishes a connection between the scattering process in infinite volume and the finite volume spectrum of the system [41]. For multi-channel scattering, the advantages and practicality of HEFT have been demonstrated in studies of various resonances, including the Roper [42, 43], the $\Lambda(1405)$ [44], the $N^*(1535)$ [45] and the $D_s^*(2317/2460)$ [46]. Because the Hamiltonian operates within the Fock space, effectively describing interactions among various different channels, the HEFT approach has two important features. 1) It provides insight into the composition of the eigenstates through the strength of various components of the eigenvectors. 2) It also enables an examination of the quark-mass dependence of resonance properties in a single formalism, enabling this unified analysis.

Here, we consistently analyze the spectra provided by several different LQCD collaborations using the HEFT framework, drawing on results extracted in the rest frame [47], moving frame and elongated frames [48]. Motivated by the physical picture mentioned, the Hamiltonian employed here is studied within a framework that involves a bare ρ , as well as $\pi\pi$ and $\omega\pi$ channels. We obtain the bare ρ mass in various regularization schemes from the lattice energy levels and investigate its dependence on m_π . We observe that the linear slope of the bare ρ mass with respect to m_π^2 is minimally affected by scheme dependence. Furthermore, we investigate the composition of the ρ meson, using the eigenvector of the

eigen-energy state closest to the physical ρ mass. Finally, we illustrate interesting discrepancies in contemporary lattice QCD calculations.

The paper is organized as follows. In Sec. II we provide an overview of the HEFT formulation and proceed to construct the finite volume Hamiltonian for the specific case under investigation. Section III presents the results of the numerical analysis and examines the dependence of various variables on m_π . Finally, in Sec. IV, we draw the discussion to a close with a concise summary and a suggestions for further analysis.

II. FORMALISM

A. Hamiltonian model

The Hamiltonian in the center of mass frame of the interacting system is divided into two parts as follows,

$$H = H_0 + H_I, \quad (2)$$

where H_0 is the non-interacting part, and H_I is the interaction part. In this work, we include a bare ρ meson, which can be identified as a $q\bar{q}$ state, as well as two coupled channels, $\pi\pi$ and $\pi\omega$. In the infinite volume, characterized by $SO(3)$ symmetry, it is most convenient to express the interaction in the JLS basis defined as [49]

$$|\alpha; k^*, JM\ell S\rangle = A_\alpha \sum_{m\sigma\sigma_1\sigma_2} C_{\ell S}(JM; m\sigma) C_{s_1 s_2}(S\sigma; \sigma_1\sigma_2) \times \int d\hat{k}^* Y_{\ell m}(\hat{k}^*) |\alpha; \mathbf{k}^*, \sigma_1 \sigma_2\rangle, \quad (3)$$

where $C_{j_1 j_2}(jm; m_1 m_2)$ is the Clebsch-Gordon (CG) coefficient of the $SU(2)$ group, $Y_{\ell m}$ are the normalized spherical harmonics functions and $|\alpha; \mathbf{k}^*, \sigma_1 \sigma_2\rangle$ indicates the $\alpha = \pi\pi$ or $\pi\omega$ channels, with relative momentum \mathbf{k}^* and z -components of the spins of two particles, σ_1 and σ_2 , respectively. (For convenience, the quantities with an asterisk in this paper are all defined in the center of mass frame.) In addition, A_α is the normalization factor that equals $\frac{1}{\sqrt{2}}$ if $\alpha = \pi\pi$ and otherwise is unity, m and σ are the z -components of the orbital angular momentum and total spin, respectively, S_1 and S_2 are the spins of the particles in channel α and J , M , ℓ and S are the total angular momentum, the z -component of the total angular momentum, orbital angular momentum, and total spin, respectively. The $|\alpha; k^*, M\rangle$ is normalized as,

$$\langle \alpha; k^*, JM\ell S | \alpha'; k'^*, JM'\ell S \rangle = \frac{\delta(k^* - k'^*)}{k^{*2}} \delta_{\alpha\alpha'} \delta_{MM'}. \quad (4)$$

In general, there are interactions between the bare state and the two-particle channels as well as within and between the coupled channels. However, in this study, most of the energy levels and phase shifts are in the resonance region, so the dominant interaction is that between

the bare state and two-particle channels. In addition, given the limited data concerning the energy levels from LQCD as well as experimental observables, we find that, in practice, the existing data can be described well without introducing channel-channel interactions. For this reason, the $\pi\pi - \pi\pi$, $\pi\pi - \pi\omega$ and $\pi\omega - \pi\omega$ t/u-channel interactions are neglected.

Because of the definite J^P quantum number of the bare ρ meson, it is sufficient to focus on the Hamiltonian in the subspace spanned by $|\alpha = \pi\pi; k^*, J = 1, M, \ell = 1, S = 0\rangle$ and $|\alpha = \omega\pi; k^*, J = 1, M, \ell = 1, S = 1\rangle$. For convenience, the JLS indices will be suppressed hereafter.

The free energy part of the Hamiltonian in this subspace, H_0 , is given by,

$$H_0 = \sum_M m_\rho^B |\rho_B, M\rangle \langle \rho_B, M| + \sum_{\alpha, M} \int k^{*2} dk^* (E_{\alpha_1}(k^*) + E_{\alpha_2}(k^*)) |\alpha; k^*, M\rangle \langle \alpha; k^*, M|, \quad (5)$$

where $|\rho_B, M\rangle$ indicates the bare ρ state with z -component of spin, M , $E_{\alpha_i}(k) = \sqrt{k^2 + m_{\alpha_i}^2}$ with $\alpha_i = \pi$ or ω , m_{α_i} is for the mass of the particle in the α channel and m_ρ^B is the mass of the bare single-particle basis state.

The interacting part, H_I , is given within the model by,

$$H_I = \sum_{\alpha, M} \int k^{*2} dk^* \{ V_\alpha(k^*) |\rho_B, M\rangle \langle \alpha; k^*, M| + \text{h.c.} \}, \quad (6)$$

where the interaction term V_α is independent of M , as a consequence of the Wigner-Eckart theorem, and given by

$$V_{\pi\pi}(k^*) = \frac{g_{\rho\pi\pi}}{2\pi\sqrt{3}} \frac{k^*}{\sqrt{m_\rho^B E_\pi(k^*)}} u_{\pi\pi}(k^*), \quad (7)$$

$$V_{\omega\pi}(k^*) = \frac{g_{\omega\rho\pi}}{2\pi\sqrt{6}} \frac{k^* \sqrt{m_\rho^B}}{\sqrt{E_\pi(k^*) E_\omega(k^*)}} u_{\omega\pi}(k^*), \quad (8)$$

where $u_{\pi\pi}$ and $u_{\omega\pi}$ are the form factors parameterizing the internal structure of hadrons and ensuring the convergence of loop integrals. Here, the usual dipole form factors are used [50, 51],

$$u_{\pi\pi}(k) = \left(\frac{\Lambda_{\rho\pi\pi}^2}{k^2 + \Lambda_{\rho\pi\pi}^2} \right)^2, \quad (9)$$

$$u_{\omega\pi}(k) = \left(\frac{\Lambda_{\omega\rho\pi}^2 - \mu_\pi^2}{k^2 + \Lambda_{\omega\rho\pi}^2} \right)^2, \quad (10)$$

where $\mu_\pi = 138.5\text{MeV}$ is the physical mass of the pion.

The scattering T-matrix, defined by $S_{fi} = \delta_{fi} - 2\pi i \delta^4(p_f - p_i) T_{fi}$, can be obtained from the partial wave Lippmann-Schwinger equation [41, 50, 52],

$$T_{\alpha\beta}(p, q, E) = V_{\alpha\beta}(p, q, E) + \sum_\gamma \int k^2 dk \frac{V_{\alpha\gamma}(p, k, E) T_{\gamma\beta}(k, q, E)}{E - E_{\gamma_1}(k) - E_{\gamma_2}(k) + i\varepsilon}, \quad (11)$$

where $V_{\alpha\beta}$ comes from bare ρ exchange in the s -channel and is given by

$$V_{\alpha\beta}(p, q, E) = \frac{V_\alpha^*(p) V_\beta(q)}{E - m_\rho^B}. \quad (12)$$

with V_α defined in Eqs.(7) and (8). In the present case $T_{\pi\pi, \pi\pi}(p, q; E)$ can be obtained analytically

$$T_{\pi\pi, \pi\pi}(p, q; E) = V_{\pi\pi}^*(p) G(E) V_{\pi\pi}(q), \quad (13)$$

where $G(E)$ is the full propagator of the ρ meson defined by,

$$G(E)^{-1} = E - m_\rho^B - \Sigma(E), \quad (14)$$

with the self-energy

$$\Sigma(E) = \Sigma_{\pi\pi}(E) + \Sigma_{\omega\pi}(E), \quad (15)$$

$$\Sigma_{\pi\pi}(E) = \int q^2 dq \frac{|V_{\pi\pi}(q)|^2}{E - 2E_\pi(q) + i\varepsilon}, \quad (16)$$

$$\Sigma_{\omega\pi}(E) = \int q^2 dq \frac{|V_{\omega\pi}(q)|^2}{E - E_\pi(q) - E_\omega(q) + i\varepsilon}. \quad (17)$$

The partial-wave phase shift, $\delta(E)$, for the P -wave $\pi\pi \rightarrow \pi\pi$ elastic scattering is then given by,

$$e^{2i\delta(E)} = 1 - i \frac{\pi \bar{p} E}{2} \bar{p} T_{\pi\pi, \pi\pi}(\bar{p}, \bar{p}; E), \quad (18)$$

$$\delta(E) = \arctan \left[\frac{\text{Im} \Sigma_{\pi\pi}(E)}{E - m_\rho^B - \text{Re} \Sigma(E)} \right] \pmod{\pi}, \quad (19)$$

where $\bar{p} = \sqrt{E^2/4 - m_\pi^2}$ is the on-shell momentum. The pole position of the ρ -resonance is located in the lower half plane of the unphysical Riemann sheet of the $\pi\pi$ -channel but the first Riemann sheet of the $\omega\pi$ -channel and determined by solving the equation

$$0 = E - m_\rho^B - \Sigma(E). \quad (20)$$

B. The Hamiltonian in finite volume

To obtain the energy levels in finite volume, we need to construct the finite volume Hamiltonian (FVH). Two major problems are encountered. Firstly, the correspondence between the Fock spaces spanned by the states with continuous and discrete momentum and secondly, the symmetry is reduced from the $O(3)$ group to a finite subgroup, G , for the finite volume. As a result, J and M are no longer good quantum numbers. In Refs.[47, 48], the standard formalism for the rest, moving and elongated frames were presented. Here we give a brief introduction to those aspects relevant to the present work.

To obtain the FVH in terms of the states with discrete momentum, one needs to make the following substitutions in Eqs.(5) and (6). First one sets

$$|\rho_B, M\rangle \rightarrow |\rho_B, M\rangle_L, \quad (21)$$

because the bare ρ single-particle state does not change. However, it is very different for the two-particle state,

$$|\alpha; k^*, M\rangle \rightarrow \sqrt{\frac{V}{(2\pi)^3}} |\alpha; e_{\mathbf{n}}, M\rangle, \quad (22)$$

and

$$\int d^3 \mathbf{k}^* \rightarrow \frac{(2\pi)^3}{V} \sum_{\mathbf{n} \in \mathbb{Z}^3}, \quad (23)$$

where $V = \eta L^3$ is the volume of the box, with elongation factor η , and $e_{\mathbf{n}}$ denotes a degenerate shell of the non-interacting Hamiltonian in the rest frame, because those states with the same $e_{\mathbf{n}}$ share the same $|\mathbf{k}^*(\mathbf{n})|$. For example, in the rest frame of a cubic box, $\mathbf{k}^* = \frac{2\pi}{L} \mathbf{n}$ and hence $e_{\mathbf{n}} = \mathbf{n}^2$. However, for the general case, $\mathbf{k}^*(\mathbf{n})$ and hence $e_{\mathbf{n}}$ are not that simple. A detailed discussion of $e_{\mathbf{n}}$ and $\mathbf{k}^*(\mathbf{n})$ can be found in Ref. [48] and a summary is given in Appendix A. The finite volume basis vector, $|\alpha; e_{\mathbf{n}}, M\rangle$, is given by an expression analogous to Eq. (3)

$$|\alpha; e_{\mathbf{n}}, M\rangle = A_{\alpha} \sum_{m\sigma_1\sigma_2} C_{\ell S}(JM; m\sigma) C_{s_1 s_2}(S\sigma; \sigma_1\sigma_2) \times \sum_{\mathbf{n} \in \{\hat{e}_{\mathbf{n}}\}} Y_{\ell m}(\hat{\mathbf{k}}^*(\mathbf{n})) |\mathbf{k}^*(\mathbf{n}), \sigma_1\sigma_2\rangle, \quad (24)$$

with $J = 1$, $\ell = 1$ and $S = 0/1$ for $\alpha = \pi\pi/\omega\pi$, respectively. Here $\{\hat{e}_{\mathbf{n}}\}$ denotes the set of integer vectors with the same $e_{\mathbf{n}}$.

Note that the states defined in Eq. (3) with different values of $JM\ell S$ are orthogonal, which is not the case in the finite volume since $O(3)$ symmetry is broken. Thus, it is necessary to construct an orthogonal basis $|\alpha; e_{\mathbf{n}}, \Gamma, a\rangle$ furnishing an irreducible representation Γ of G . Such states take linear combinations of the basis states $|\alpha; e_{\mathbf{n}}, M\rangle$ with reduction coefficients $C_{\Gamma, G}$ [48, 53],

$$|\alpha; e_{\mathbf{n}}, \Gamma, a\rangle := \sqrt{\frac{1}{Z_{\Gamma}(e_{\mathbf{n}})}} [C_{\Gamma, G}]_{M, a} |\alpha; e_{\mathbf{n}}, M\rangle, \quad (25)$$

$$\langle \alpha; e_{\mathbf{n}}, \Gamma, a | \alpha'; e'_{\mathbf{n}}, \Gamma', a' \rangle = \delta_{\alpha\alpha'} \delta_{e_{\mathbf{n}} e'_{\mathbf{n}}} \delta_{\Gamma\Gamma'} \delta_{aa'}, \quad (26)$$

where $Z_{\Gamma}(e_{\mathbf{n}})$ is the normalization factor. In general there should be another index denoting the multiplicity of Γ , but in the present case that additional index is always 1 and hence it will be suppressed. The reduction coefficients relevant to the work reported here are shown in Appendix C. Similarly,

$$|\rho_B, \Gamma, a\rangle = [C_{\Gamma, G}]_{M, a} |\rho_B, M\rangle_L, \quad (27)$$

satisfying

$$\langle \rho_B, \Gamma, a | \rho_B, \Gamma', a' \rangle = \delta_{\Gamma\Gamma'} \delta_{aa'}. \quad (28)$$

With these well-defined orthogonal basis states $|\rho_B, \Gamma, a\rangle$ and $|\alpha; e_{\mathbf{n}}, \Gamma, a\rangle$, the FVH in the rest frame for a given irreducible representation, Γ , (note that because

of the Wigner-Eckart theorem, the eigenvalue is independent of the “ a ” index, which is therefore suppressed) is given by

$$H^{\text{fin}} = \sum_{\Gamma} (H_{0, \Gamma}^{\text{fin}} + H_{I, \Gamma}^{\text{fin}}), \quad (29)$$

$$H_{0, \Gamma}^{\text{fin}} = m_{\rho}^B |\rho_B, \Gamma\rangle \langle \rho_B, \Gamma| + \sum_{\alpha; e_{\mathbf{n}}} |\alpha; e_{\mathbf{n}}, \Gamma\rangle \langle \alpha; e_{\mathbf{n}}, \Gamma| \times (E_{\alpha_1}(|\mathbf{k}^*(\mathbf{n})|) + E_{\alpha_2}(|\mathbf{k}^*(\mathbf{n})|)), \quad (30)$$

$$H_{I, \Gamma}^{\text{fin}} = \sum_{\alpha, e_{\mathbf{n}}} V_{\alpha, \Gamma}^{\text{fin}}(|\mathbf{k}^*(\mathbf{n})|) |\rho_B, \Gamma\rangle \langle \alpha; e_{\mathbf{n}}, \Gamma| + \text{h.c.} \quad (31)$$

Alternatively, these equations may be expressed in matrix form

$$H_{0\Gamma}^{\text{fin}} + H_{I\Gamma}^{\text{fin}} = \begin{pmatrix} m_{\rho}^B & v^{\text{T}} \\ v & h_0 \end{pmatrix} \quad (32)$$

$$v^{\text{T}} = (V_{\pi\pi, \Gamma}^{\text{fin}}(|\mathbf{k}^*(\mathbf{n}_1)|), V_{\pi\pi, \Gamma}^{\text{fin}}(|\mathbf{k}^*(\mathbf{n}_2)|), \dots, \dots, V_{\omega\pi, \Gamma}^{\text{fin}}(|\mathbf{k}^*(\mathbf{n}'_1)|), V_{\omega\pi, \Gamma}^{\text{fin}}(|\mathbf{k}^*(\mathbf{n}'_2)|), \dots) \quad (33)$$

$$h_0 = \text{diag}(2E_{\pi}(|\mathbf{k}^*(\mathbf{n}_1)|), 2E_{\pi}(|\mathbf{k}^*(\mathbf{n}_2)|), \dots, E_{\pi}(|\mathbf{k}^*(\mathbf{n}'_1)|) + E_{\omega}(|\mathbf{k}^*(\mathbf{n}'_1)|), E_{\pi}(|\mathbf{k}^*(\mathbf{n}'_2)|) + E_{\omega}(|\mathbf{k}^*(\mathbf{n}'_2)|), \dots). \quad (34)$$

In principle the FVH is countably infinite-dimensional, while in practice it is found that the contribution of high-energy states to the low-lying eigenvalues of interest is negligible. Therefore, the matrix can be truncated by excluding the states with momentum higher than a certain value k_{cut}^* to obtain a finite-dimensional matrix.

By comparing Eqs.(3),(6),(24),(25) and (31), $V_{\alpha, \Gamma}^{\text{fin}}(|\mathbf{k}^*(\mathbf{n})|)$ is written as,

$$V_{\alpha, \Gamma}^{\text{fin}}(e_{\mathbf{n}}) = \sqrt{\frac{(2\pi)^3}{V}} J_{\alpha}(e_{\mathbf{n}}) \sqrt{Z_{\Gamma}(e_{\mathbf{n}})} V_{\alpha}(|\mathbf{k}^*(\mathbf{n})|), \quad (35)$$

where the Jacobian, J_{α} , just appears for a moving system, with the expression shown in Eq. (A2).

C. Fitting Formulas

In the present work, we fit the eigenvalues of the FVH, E^{H} , to the lattice spectrum, $E_{\text{cm}}^{\text{lat}}$, with the usual least- χ^2 strategy. That is, we minimize the χ^2 defined as

$$\chi^2 = (E^{\text{H}} - E_{\text{cm}}^{\text{lat}})^{\text{T}} \mathbb{C}^{-1} (E^{\text{H}} - E_{\text{cm}}^{\text{lat}}), \quad (36)$$

where \mathbb{C} denotes the covariance matrix of the lattice spectrum. It should be noted that $E_{\text{cm}}^{\text{lat}}$ is the spectrum that has been transformed into the rest frame. If a certain energy level, E_n^{lat} , is extracted from the composite operator with $\mathbf{P} \neq 0$, it needs to be converted to $E_{\text{cm}, n}^{\text{lat}}$ through

$$E_{\text{cm}, n}^{\text{lat}} = \sqrt{(E_n^{\text{lat}})^2 - \mathbf{P}^2}. \quad (37)$$

In our model, there are five parameters, including the bare mass, m_{ρ}^B , two coupling constants $g_{\rho\pi\pi}$ and $g_{\omega\rho\pi}$, defined in Eqs. (7) and (8), and two cut-off parameters $\Lambda_{\rho\pi\pi}$ and $\Lambda_{\omega\rho\pi}$, defined in Eqs. (9) and (10), respectively.

D. Formulas for the m_π dependence

To extrapolate the results of the lattice calculations to the physical region, one needs to investigate the m_π -dependence of the properties of the ρ meson. This issue has been previously discussed in some studies [51, 54–59] and in this paper it will be studied within the framework of HEFT. As discussed in Ref. [55], in the framework of Chiral Perturbation Theory, the mass of the ρ is a function of m_π of the form

$$m_\rho^{\text{P}} = c'_0 + c'_1 m_\pi^2 + c'_2 m_\pi^3 + c'_3 m_\pi^4 \ln\left(\frac{m_\pi^2}{m_\rho^2}\right) + \mathcal{O}(m_\pi^4), \quad (38)$$

where m_ρ^{P} is related to the pole mass of the ρ , corresponding to the real part of the pole of the T-matrix in the complex plane. In general, m_ρ^{P} is different from the usual Breit-Wigner mass, m_ρ^{BW} , which is defined as the real energy at which the phase shift is 90 degrees. For the present case, however, the difference is negligible.

As discussed in Refs. [51, 55], the quark mass insertion at tree level only contributes to the m_π^2 term in Eq. (38) up to $\mathcal{O}(m_\pi^4)$, with the other two terms arising from pion-loop self energies. The m_π^3 term comes from the $\omega\pi$ loop, involving a vector-vector-pseudoscalar (VVP) vertex, while both $\pi\pi$ and $\omega\pi$ loops contribute to the log term. Within the present framework, the pole of the T-matrix is determined by Eq. (20), which tells us that

$$m_\rho^{\text{P}} = m_\rho^{\text{B}} + \text{Re} \Sigma(m_\rho^{\text{P}} - i\Gamma/2). \quad (39)$$

where $m_\rho^{\text{P}} - i\Gamma/2$ is the complex pole position solved from Eq. (20). Comparing Eq. (38) and Eq. (39), the bare mass m_ρ^{B} is a quadratic function of m_π at the leading order,

$$m_\rho^{\text{B}}(m_\pi) = c_0 + c_1 m_\pi^2. \quad (40)$$

In our analysis, this equation will be used to study the extracted m_ρ^{B} as function of m_π .

It is important to note that Eq. (40) is derived from the continuum field theory. In principle, to extrapolate the results obtained from lattice, the residual lattice artifacts should be estimated and removed. Since all actions are $O(a)$ -improved, the effect of the finite lattice spacing can be estimated from $O(a^2)$ as

$$m_\rho^{\text{B}}(m_\pi; a) = c_0 + c_1 m_\pi^2 + \xi a^2, \quad (41)$$

where ξ characterizes the rate at which it approaches the continuum limit and may vary from collaboration to collaboration as different fermion actions are used.

E. Model (in)dependence in HEFT

Understanding the model-dependent and model-independent aspects of HEFT is important. As HEFT

incorporates the Lüscher formalism [41, 60], there are aspects of the calculation that share the same level of model independence as the Lüscher formalism itself.

1. Model independence

In particular, the Lüscher formalism provides a rigorous relationship between the finite volume energy spectrum and the scattering phase shifts and inelasticities of infinite-volume experiment. In HEFT, this relationship is mediated by a Hamiltonian. When the parameters of the Hamiltonian are sufficient to provide a high-quality description of lattice QCD results, then the associated scattering amplitudes are of high quality. The key is to have a sufficient number of tunable parameters to accurately describe the lattice QCD results.

In the baryon sector, high-quality lattice QCD results are scarce and HEFT is often fit to experimental data first. The HEFT formalism then describes the finite-volume dependence of the hadronic spectrum, indicating where future lattice QCD results will reside.

Fortunately, in the ρ -meson channel relevant to this analysis, several lattice QCD groups have resolved the finite-volume spectrum, taking care to assess the subtle shifts in the spectrum associated with avoided level crossings in the finite volume. This information is central to the Lüscher formalism and as such, is central to the HEFT analysis presented here. We will show excellent fits to the lattice QCD results such that HEFT provides rigorous predictions of the scattering observables with model independence at the level of the Lüscher formalism.

Of course, this model independence is restricted to the case of matched quark masses in finite-volume and infinite-volume. The Lüscher formalism provides no avenue for changing the quark mass. In other words, to make contact with experiment, the quark masses used in the lattice QCD simulations must be physical.

On the other hand, χ PT is renowned for describing the quark mass dependence of hadron properties in a model-independent manner, provided one employs the truncated expansion in the power-counting regime, where higher-order terms not considered in the expansion are small by definition. Given that finite-volume HEFT reproduces finite-volume χ PT in the perturbative limit by construction [60, 61], it is reasonable to explore the extent to which this model independence persists in the full nonperturbative calculation of HEFT.

This was explored in Ref. [61]. In the one channel case where a single particle basis state (e.g. a quark-model like Δ) couples to one two-particle channel (e.g. πN), the independence of the results on the form of regularisation is reminiscent of that realised in χ PT. Any change in the regulator is absorbed by the low-energy coefficients such that the renormalised coefficients are physical, independent of the renormalisation scheme.

However, in the more complicated two-channel case

with a $\pi\Delta$ channel added, the same was not observed. The form of the Hamiltonian becomes constrained, describing experimental data accurately for only a limited range of parameters. The Hamiltonian becomes a model in this case, with regulator-function scales and shapes governed by the experimental data. The principles of chiral *perturbation* theory no longer apply in this nonperturbative calculation. However, for fit parameters that describe the data well, the model independence of the Lüscher formalism remains intact. The Hamiltonian is only mediary.

2. Quark mass variation

The consideration of variation of the quark masses away from the physical point provides further constraints on the Hamiltonian. In particular, lattice QCD results away from the physical point provide new constraints on the form of the Hamiltonian. In the two-channel case, the Hamiltonian becomes tightly constrained when considering experimental scattering data and lattice QCD results together.

With the Hamiltonian determined by one set of lattice results, one can then make predictions of the finite-volume spectrum considered by other lattice groups at different volumes and different quark masses. For the cases considered in the baryon spectrum the predictions of HEFT are in agreement with lattice QCD spectrum predictions. For example, in the Δ -channel HEFT successfully predicts the finite-volume spectrum of the CLS consortium [61, 62]. In the $N(\frac{1}{2}^+)$ channel, HEFT reproduces the lattice QCD results from Lang *et al.* [43, 63]. In the $N(\frac{1}{2}^-)$ channel, HEFT successfully predicts spectra from the CLS consortium [64, 65], the HSC [64, 66, 67] and Lang & Verducci [64, 68]. Thus one concludes that the systematic errors of the HEFT approach to quark-mass variation are small on the scale of contemporary lattice QCD uncertainties. As the Hamiltonian is constrained by model-independent scattering data and lattice QCD results, we expect this success to be realised in the ρ -meson channel.

Variation in the quark mass is conducted in the same spirit as for χ PT. The couplings are held constant and the hadron masses participating in the theory take values as determined in lattice QCD. The single-particle bare basis state acquires a quark mass dependence and this is done in the usual fashion by drawing on terms analytic in the quark mass. In most cases, lattice QCD results are only able to constrain a term linear in m_π^2 , but on occasion, the data can demand a small m_π^4 contribution.

In the present analysis, we will see that the accuracy of contemporary lattice QCD results for the ρ -meson spectrum is sufficient to consider only a term linear in m_π^2 . Even then we show that there are incompatibilities between the lattice QCD results. Contrary to the baryon sector, we show how a Hamiltonian constrained by the results of one group is incompatible with the results of

other groups. Referring back to the model-independence of the Lüscher relation embedded within HEFT, the spectra of one group leads to scattering observables that are incompatible with the predictions of other groups.

The model independence associated with the movement of quark masses away from the physical point is largely governed by the distance one chooses to move from the physical quark-mass point. The HEFT approach is systematically improvable, reliant on high-quality lattice QCD results to constrain the higher-order terms that one can introduce. In addition to the aforementioned analytic m_π^4 term, one could also include higher-order interaction terms from the chiral Lagrangian. However, this increased level of precision is not yet demanded by contemporary lattice QCD results.

3. Model dependence

Now that the Hamiltonian has become a tightly constrained model, the eigenvectors describing the manner in which the non-interacting basis states come together to compose the eigenstates of the spectrum are model dependent. At the same time, there is little freedom in the model parameters of the Hamiltonian such that the predictions of the Hamiltonian are well defined.

With regard to the bare mass, there is interplay between the multi-particle channels included in the calculation, the regularisation scales considered and the associated bare mass. For example, as will be seen, upon introducing the additional $\omega\pi$ channel, one observes an increase in the bare mass as some of this contribution is carried by the $\omega\pi$ contribution. Thus the bare mass is defined only when the number of channels and their regularisation scales are fixed within the model. With the channels selected and preferred regularisation scales set, the bare mass becomes well-defined within the model.

While the bare mass is model dependent, we will show that the slope of the bare mass as a function of quark mass is insensitive to the number of two-particle channels considered. As such, this observation may be of assistance to those developing quark models.

Returning to the eigenvectors of the Hamiltonian, we emphasise that the parameters of the Hamiltonian model are well constrained, such that the predictions of the model are well defined.

The information contained in the Hamiltonian eigenvectors describing the basis-state composition of finite-volume energy eigenstates is analogous to the information contained within the eigenvectors of lattice QCD correlation matrices describing the linear combination of interpolating fields isolating energy eigenstates on the lattice. These too are model dependent, governed by the nature of the interpolating fields used to construct the correlation matrix.

What is remarkable is that with a suitable renormalisation scheme on the lattice (e.g. interpolators are normalised to set diagonal correlators equal to 1 at one slice

after the source), the composition of the states drawn from the lattice correlation matrix is very similar to the description provided by HEFT [43, 64]. While both eigenvector sets are model dependent, their similarity does indeed provide some relevant insight into hadron structure. And because regularisation in the Hamiltonian is tightly constrained, one can begin to separate out the contributions of bare versus two-particle channels, something that is impossible in χ PT.

4. Summary

In summary, there is a direct model-independent link between the finite-volume spectrum calculated at physical quark masses and the scattering observables of experiment. This model independence is founded on the Lüscher formalism embedded with HEFT. Similarly, variation of the quark masses away from the physical quark mass has systematic uncertainties that are small relative to contemporary lattice QCD spectral uncertainties. Finally, the Hamiltonian eigenvectors describing the basis-state composition of finite-volume energy eigenstates are model dependent. They are analogous to the interpolator dependent eigenvectors of lattice QCD correlation matrices describing the linear combination of interpolating fields isolating energy eigenstates on the lattice. The similarity displayed by these two different sets of eigenvectors suggests that they do indeed provide insight into hadron structure.

III. NUMERICAL RESULTS AND DISCUSSION

A. The LQCD Data

The finite volume spectra for the $I = \ell = 1$ $\pi\pi$ sector with dynamical fermions at various pion masses have been provided by several LQCD collaborations over the past decade, including PACS-CS (2011, $N_f = 2+1$) [24], HSC (2013, $N_f = 2+1$) [27], HSC (2015, $N_f = 2+1$) [26], Guo *et al.* (2016, $N_f = 2$) [32], MILC(2016, $N_f = 2+1$) [33], C. Alexandrou *et al.* (2017, $N_f = 2+1$) [29], J. Bulava *et al.* (2019, $N_f = 2+1$) [34], and ETMC (2020, $N_f = 2+1(+1)$) [28]. Further details and energy levels are shown in Table I and the panels in Fig. 1, as well as all figures in Appendix D, where HEFT is fit to the various lattice data sets.

B. Three Fitting Schemes

In this work, our aim is to study the properties of the ρ meson by investigating the pion mass dependence of various relevant variables. In the HEFT framework, we have five free parameters which may be used to fit the lattice data with different pion masses. However, for each specific pion mass, there are only a few energy levels.

In addition, the $\omega\pi$ contribution is considerably weaker than that of the $\pi\pi$ channel, since the threshold of $\omega\pi$ is higher than the ρ mass. Consequently, we first adopt scheme A, wherein the interaction $V_{\omega\pi}$ is turned off, i.e., $g_{\omega\rho\pi} \equiv 0$, while m_ρ^B , $g_{\rho\pi\pi}$, and $\Lambda_{\rho\pi\pi}$ are treated as free fitting parameters. The finite volume spectra provided by various collaborations involving different π masses are each fit independently. Using scheme A, it is found that both $g_{\rho\pi\pi}$ and $\Lambda_{\omega\rho\pi}$ show a very weak dependence on m_π , while m_ρ^B is strongly dependent on m_π , as anticipated earlier.

Building upon the results found using scheme A, in scheme B both $g_{\rho\pi\pi}$ and $\Lambda_{\rho\pi\pi}$ are fixed to be independent of m_π , in accord with standard practice in chiral effective field theory. m_ρ^B is allowed to vary. As a result, this approach effectively combines spectra from various pion masses provided by different LQCD groups together in a unified analysis to constrain the variation of the bare mass, m_ρ^B , with m_π .

Finally, the contribution of the $\omega\pi$ channel is examined in scheme C. In this case $V_{\omega\pi}$ is switched on, however, the two coupling constants, $g_{\rho\pi\pi}$ and $g_{\omega\rho\pi}$, as well as two cutoffs, $\Lambda_{\rho\pi\pi}$ and $\Lambda_{\omega\rho\pi}$, are taken to be independent of m_π , while only m_ρ^B is permitted to vary in the fitting. These three schemes are summarized in Table II.

C. Fitting Results

1. Results for Scheme A

Recall that in scheme A, the $\rho - \omega\pi$ interaction is turned off and the lattice spectra are fit using three free parameters m_ρ^B , $g_{\rho\pi\pi}$, and $\Lambda_{\rho\pi\pi}$. The fitted spectra as a function of spatial extent, L , are shown by the blue curves in Fig. 1 for $m_\pi = 200$ MeV as an illustration. All other fits are presented in Appendix D. The corresponding fitted parameter values are outlined in the columns dedicated to scheme A in Table III. In addition, the pion mass dependence of the three parameters, $g_{\rho\pi\pi}$, $\Lambda_{\rho\pi\pi}$, and m_ρ^B are shown in Fig. 2 and in the top panel of Fig. 3, respectively.

From Fig. 2, it is found that the cut-off parameter $\Lambda_{\rho\pi\pi}$ and the dimensionless coupling constant, $g_{\rho\pi\pi}$, both show a weak dependence on m_π . In contrast, it is worth noting that for each m_π , $\Lambda_{\rho\pi\pi}$ exhibits a large uncertainty. Indeed, in some cases the upper uncertainty does not display in MINUIT2, which means that even for very large values of the cut-off, we can still find a reasonable fit for the energy levels. This observation suggests that the eigenvalue of the FVH around the region of the ρ mass is insensitive to $\Lambda_{\rho\pi\pi}$. This is consistent with the findings reported in Ref. [61], where the Λ -dependence of the eigenvalue and eigenvector are investigated in detail. A more common [27] dressed coupling constant, $g_{\rho\pi\pi}^{BW}$, is

TABLE I. Details of the spectra by different collaborations. Columns, from left to right, show collaboration and year of spectra, pion mass (m_π), number of flavor (N_f), lattice size (L) and spacing (a) in fm, employed gauge and fermion actions, number of energy levels (N_{lvl}), and energy level extraction method. Besides, the spectra provided by Guo *et al.* are extracted in a elongated box with factor $\eta = 1, \frac{7}{6}, \frac{4}{3}$ for $m_\pi = 226$ MeV, and $\eta = 1, 1.25, 2$ for $m_\pi = 315$ MeV.

COLLAB.(Year)	m_π (MeV)	N_f	L (fm)	a (fm)	Action	N_{lvl}	method
J.Bulava(2018)	200	2+1	4.1	0.06	improved Lüscher-Weisz gauge improved Wilson fermion	17	GEVP
	220		4.1	0.09		21	
	280		3.1	0.06		15	
HSC(2013)	391	2+1	1.9	0.12	Symanzik-improved gauge anisotropic Clover fermion	7	GEVP
			2.4	0.12		10	
			2.9	0.12		14	
HSC(2015)	236		3.8	0.12		23	
HSC(2023)	330		2.8	0.12		17	
MILC(2016)	176	2+1	5.4	0.09	improved Lüscher-Weisz gauge staggered fermion	9	GEVP
	247		3.4	0.09		9	
	248		3.4	0.09		9	
	301		2.7	0.09		9	
	346		2.4	0.09		7	
	276		3.7	0.12		9	
ETMC(2020)	322	2+1+1	2.8	0.09	Iwasaki gauge twisted-mass Wilson fermion	18	GEVP
	386		2.1	0.09		16	
	262		2.6	0.08		13	
	302		3.9	0.08		23	
	376		2.6	0.08		14	
C.Alexandru(2017)	316	2+1	3.6	0.11	Symanzik-improved gauge clover Wilson fermion	15	GEVP
PACS-CS(2011)	411	2+1	2.9	0.09	Iwasaki gauge improved Wilson fermion	6	Exp Fit
Guo(2016)	226	2	2.9	0.12	Lüscher-Weisz gauge nHYP-smearred Clover fermion	8	GEVP
	315					20	

TABLE II. Outline of the fitting schemes.

	m_ρ^B	$g_{\rho\pi\pi}, \Lambda_{\rho\pi\pi}$	$g_{\omega\rho\pi}, \Lambda_{\omega\rho\pi}$
A	free	free	off
B	free	fixed	off
C	free	fixed	fixed

defined by

$$g_{\rho\pi\pi}^{\text{BW}} \equiv \sqrt{\frac{6\pi(m_\rho^{\text{BW}})^2}{\bar{p}}} \Gamma_{\rho \rightarrow \pi\pi}^{\text{BW}}, \quad (42)$$

where \bar{p} is defined by $2\sqrt{\bar{p}^2 + m_\pi^2} = m_\rho^{\text{BW}}$ and $\Gamma_{\rho \rightarrow \pi\pi}^{\text{BW}}$ is the partial width of the resonance in the Breit Wigner parameterizations. In our model, $g_{\rho\pi\pi}^{\text{BW}}$ depends on both the value of $g_{\rho\pi\pi}$ and the form factor $u_{\pi\pi}$, which is determined by $\Lambda_{\rho\pi\pi}$. As a result, the slight m_π -dependence seen in $g_{\rho\pi\pi}$ and $\Lambda_{\rho\pi\pi}$ clearly implies that the value of $g_{\rho\pi\pi}^{\text{BW}}$, approximated to be around 6.0, remains independent of m_π . This conclusion is consistent with the discussions presented in prior works, such as Refs. [29, 31, 33].

In contrast, the m_π -dependence of m_ρ^B suffers a large fluctuation, as illustrated in the top section of Fig. (3). This behavior stems from the limited number of energy

levels available for each pion mass, coupled with the considerable uncertainties associated with $g_{\rho\pi\pi}$ and $\Lambda_{\rho\pi\pi}$. In order to reduce the uncertainty associated with the bare mass, one needs to find an appropriate method to combine the analysis of the various energy levels. Inspired by the weak dependence on m_π , as well as the sizable uncertainties of $g_{\rho\pi\pi}$ and $\Lambda_{\rho\pi\pi}$, we choose these two parameters to be constant for all pion masses and re-fit each spectrum using only one single parameter, m_ρ^B .

2. Results for Scheme B

The first task is to determine the constant values of $g_{\rho\pi\pi}$ and $\Lambda_{\rho\pi\pi}$ which will be used in the analysis of the data for all values of m_π . To do that, we investigate $m_\pi = 236, 280, 322, 376, 386, 391$ MeV cases, which have the highest values of the chi-squared per degree of freedom, $\hat{\chi}^2 (= \chi^2/\text{dof})$, in scheme A. We present the distribution of the sum of the these $\hat{\chi}^2$ with respect to some fixed $g_{\rho\pi\pi}$ and $\Lambda_{\rho\pi\pi}$ in Fig. 4. It is straightforward to find the preferred values of the coupling and cutoff from this distribution. It leads us to choose the values at the black point, where $g_{\rho\pi\pi} = 7.07$ and $\Lambda_{\rho\pi\pi} = 890$

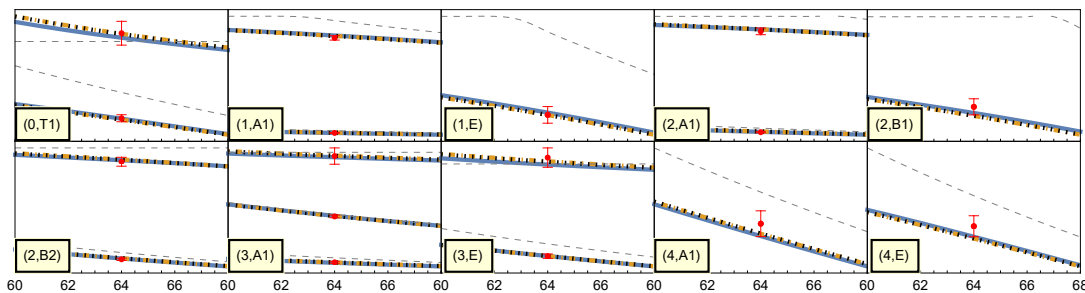


FIG. 1. Spectra with $m_\pi = 200$ MeV provided by Bulava *et al.* [34] along with that calculated by HEFT using the fitting results for schemes A, B and C. The x -axis represents the spatial extent L in units of lattice spacing a , while the y -axis indicates the energy level. Tick marks on the y -axis are omitted for clarity. Text within the yellow box (\mathbf{n}^2, Γ) signifies spectrum extraction using operators in representation Γ and with total momentum $\mathbf{P}^2 = (\frac{2\pi}{L})^2 \mathbf{n}^2$. Red points indicate the lattice spectrum provided by collaborations. Blue, orange dot-dashed and black dotted lines indicate the spectrum as the function of L calculated by HEFT using the fitting results of schemes A, B and C, respectively. The dashed gray lines indicate the non-interacting energy levels $2E_\pi(\mathbf{k}^*)$ and m_ρ^B (with m_ρ^B taken from Scheme A's fitting result for illustration). The turning points in the non-interacting energy levels are associated with energy crossings where the non-interacting two-particle energy becomes lower than the bare ρ -meson mass as L increases.

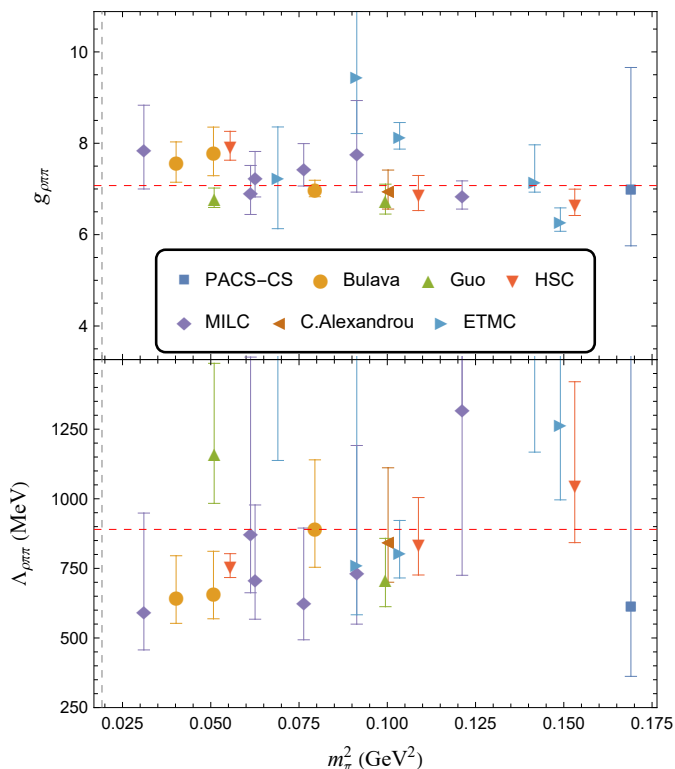


FIG. 2. m_π -dependence of $g_{\rho\pi\pi}$ and $\Lambda_{\rho\pi\pi}$ in scheme A. The dashed gray vertical line indicates the physical m_π . The dashed red horizontal lines indicate the value that will be fixed for $N_f = 2 + 1$ in scheme B.

MeV for $N_f = 2 + 1$. On the other hand, it is found that for $N_f = 2$, we should use slightly different values, namely $g_{\rho\pi\pi} = 6.75$ and $\Lambda_{\rho\pi\pi} = 950$ MeV [37, 38]. These values ensure the $\hat{\chi}^2$ satisfies the condition $\hat{\chi}^2 \lesssim 2$ for all of these values of m_π , as illustrated in Table III, in the

column of $\hat{\chi}^2$ for scheme B.

For scheme B, the curves denoting the spectra as a function of the spatial extent, L , are shown as orange dot-dashed lines in the figures in Appendix D. The fitted m_ρ^B values are presented in Fig. 3, and the columns for scheme B in Table III. Comparing Fig. 3(A) with (B), one finds that the uncertainties in m_ρ^B are significantly reduced, albeit with slight shifts in the central values. The m_π -dependence of m_ρ^B remains unclear. In particular, the values of m_ρ^B at $m_\pi = 301, 302, 315, 316$ and 322 MeV extracted from MILC, ETMC, Guo *et al.*, C. Alexandrou *et al.*, and ETMC respectively, significantly fluctuate between 840 and 920 MeV. It is apparent that there are substantial differences in the results from different LQCD groups. To address this issue, we examine the contribution of the coupling to the $\omega\pi$ [51, 55] channel, which is the closest two-particle channel in the present work and which, significantly, yields the leading non-analytic contribution to the ρ self-energy.

3. Results for Scheme C

Once $V_{\omega\pi}$ is turned on, two additional parameters, $g_{\omega\rho\pi}$ and $\Lambda_{\omega\rho\pi}$, are involved. In addition, m_ω also depends on m_π . The m_ω is not provided by most of the lattice QCD collaborations considered here. However, HSC reported a value of m_ω at $m_\pi = 391$ MeV [27]. It provides an excellent opportunity to quantify the importance of quark-mass changes. They find a ρ -meson resonance position of $a_t m_R = 0.15085(18)(3)$ in the Briet-Wigner parameterization to be compared with their stable omega mass of $a_t m_\omega = 0.15678(41)$. The difference/average is only 3.9% even at this very large pion mass. Since modern lattice QCD results are at lower quark masses, in our calculation for other collaborations, we just use the approximation $m_\omega = m_\rho^{BW}$.

TABLE III. Fitting results of schemes A, B, and C provided by the MINUIT2 program [69]. In the columns for scheme A, we show asymmetric uncertainties, since in this scheme the upper and lower uncertainties are quite different. The question mark means that some upper uncertainties are not provided by MINUIT2 since even for a very large $\Lambda_{\rho\pi\pi}$ the energy levels can still be fit well. For scheme B, $g_{\rho\pi\pi}$, and $\Lambda_{\rho\pi\pi}$ are fixed at 7.07 (6.85) and 890 (950) MeV for $N_f = 2 + 1$ (2), respectively. For scheme C, $g_{\omega\rho\pi}$ and $\Lambda_{\omega\rho\pi}$ are fixed at 18/GeV and 900 MeV, while $g_{\rho\pi\pi}$ and $\Lambda_{\rho\pi\pi}$ are fixed at 7.07 (6.85) and 900 (980) MeV for $N_f = 2 + 1$ (2), respectively. $\hat{\chi}^2$ represents the reduced chi-square, i.e. χ^2/dof with $\text{dof} = N_{\text{lvl}} - 3$ for scheme A and $N_{\text{lvl}} - 1$ for schemes B and C.

COLLAB.(Year)	m_π (MeV)	Scheme A				Scheme B		Scheme C	
		m_ρ^{B} (MeV)	$g_{\rho\pi\pi}$	$\Lambda_{\rho\pi\pi}$ (MeV)	$\hat{\chi}^2$	m_ρ^{B} (MeV)	$\hat{\chi}^2$	m_ρ^{B} (MeV)	$\hat{\chi}^2$
J.Bulava(2018)	200	$787.3^{+23.6}_{-14.8}$	$7.58^{+0.45}_{-0.43}$	$645.6^{+149.8}_{-93.0}$	0.44	819.6(4.1)	0.53	$867.7(4.5)$	0.53
	220	$795.0^{+18.6}_{-11.5}$	$7.80^{+0.55}_{-0.51}$	$662.0^{+149.4}_{-93.0}$	0.41	818.4(3.6)	0.49	$866.3(4.0)$	0.50
	280	$825.1^{+29.4}_{-14.7}$	$7.00^{+0.19}_{-0.17}$	$895.7^{+244.1}_{-141.7}$	1.07	826.2(2.4)	0.93	$870.8(2.6)$	0.97
HSC(2013)	391	$909.0^{+36.4}_{-15.5}$	$6.66^{+0.33}_{-0.24}$	$1050.3^{+370.1}_{-207.8}$	0.98	898.9(1.2)	0.97	$936.2(1.3)$	1.21
HSC(2015)	236	$829.1^{+29.4}_{-14.7}$	$7.94^{+0.32}_{-0.31}$	$756.4^{+46.4}_{-39.3}$	1.00	840.3(1.0)	1.38	$888.6(1.1)$	1.62
HSC(2023)	330	$856.1^{+13.1}_{-8.2}$	$6.89^{+0.41}_{-0.36}$	$838.6^{+165.9}_{-112.3}$	0.71	862.6(2.2)	0.78	$904.1(2.4)$	0.86
MILC(2016)	176	$806.4^{+36.3}_{-8.5}$	$7.88^{+0.96}_{-0.88}$	$596.2^{+352.5}_{-139.1}$	0.63	831.7(8.2)	0.61	$882.9(9.1)$	1.30
	247	$878.2^{+84.1}_{-21.2}$	$6.93^{+0.58}_{-0.49}$	$876.0^{+633.0}_{-213.5}$	0.73	881.3(3.9)	0.57	$928.7(4.3)$	0.53
	248	$855.8^{+28.6}_{-12.4}$	$7.27^{+0.55}_{-0.44}$	$711.7^{+266.1}_{-144.3}$	0.37	874.3(4.1)	0.35	$921.5(4.5)$	0.32
	275	$861.5^{+29.1}_{-12.5}$	$7.45^{+0.54}_{-0.39}$	$630.2^{+264.7}_{-136.7}$	0.36	886.0(5.5)	0.43	$932.4(6.0)$	0.41
	301	$916.6^{+47.2}_{-13.8}$	$7.79^{+1.15}_{-0.86}$	$735.8^{+455.7}_{-186.0}$	0.26	928.5(5.8)	0.29	$972.4(6.4)$	0.28
	346	$999.8^{+?}_{-51.9}$	$6.86^{+0.31}_{-0.30}$	$1321.0^{+?}_{-595.8}$	0.26	958.9(6.4)	0.23	$998.6(6.9)$	0.28
	376	$927.4^{+14.4}_{-10.6}$	$8.15^{+0.30}_{-0.28}$	$807.2^{+115.0}_{-91.6}$	1.20	924.4(2.6)	2.16	$967.6(2.8)$	2.06
ETMC(2020)	386	$999.6^{+59.5}_{-21.8}$	$6.30^{+0.28}_{-0.23}$	$1267.3^{+557.2}_{-271.1}$	1.32	974.1(2.2)	1.54	$1012.1(2.4)$	2.00
	262	$1156.2^{+68.7}_{-208.0}$	$7.26^{+1.10}_{-1.13}$	$2421.0^{+?}_{-1283.4}$	0.58	920.2(8.6)	0.67	$967.3(9.5)$	0.72
	302	$928.7^{+157.1}_{-23.7}$	$9.46^{+1.42}_{-1.25}$	$765.6^{+862.6}_{-182.3}$	0.56	919.1(5.8)	1.00	$964.8(6.3)$	0.99
	376	$1034.6^{+170.3}_{-51.8}$	$7.16^{+0.81}_{-0.23}$	$1571.4^{+?}_{-403.8}$	0.98	952.6(1.8)	1.57	$993.4(1.9)$	1.52
	316	$840.6^{+25.8}_{-12.7}$	$6.96^{+0.45}_{-0.40}$	$847.4^{+263.9}_{-147.1}$	0.10	846.6(2.3)	0.10	$890.1(2.5)$	0.10
PACS-CS(2011)	411	$913.0^{+185.0}_{-10.2}$	$6.97^{+2.70}_{-1.21}$	$609.0^{+?}_{-246.8}$	0.83	934.3(5.2)	0.82	$973.3(5.6)$	0.88
Guo(2016)	226	$834.4^{+43.7}_{-21.3}$	$6.79^{+0.23}_{-0.19}$	$1163.1^{+323.4}_{-179.6}$	1.69	854.3(1.4)	1.88	$806.4(1.3)$	1.78
	315	$824.1^{+11.6}_{-7.0}$	$6.75^{+0.35}_{-0.30}$	$709.5^{+148.2}_{-97.1}$	0.20	892.4(1.4)	1.50	$848.0(1.3)$	1.84

Since the threshold of $\omega\pi$ is higher than the spectrum extracted, it is expected that the $\omega\pi$ loop will shift the value of m_ρ^{B} but have a negligible influence on the resulting χ^2 .

Instead of allowing $g_{\omega\rho\pi}$ and $\Lambda_{\omega\rho\pi}$ to be two additional free parameters, we impose appropriate constraints to fix them. Two constraints are identified at the physical pion mass μ_π : the decay width, $\Gamma_{\omega \rightarrow 3\pi}$, is primarily determined by the $\omega \rightarrow \rho\pi \rightarrow 3\pi$ mechanism (which is estimated to yield around 90% [70] of the width) and the P -wave phase shifts of $\pi\pi \rightarrow \pi\pi$ in the energy region around the ρ mass.

For simplification, we take the two cut-off, $\Lambda_{\rho\pi\pi}$ and $\Lambda_{\omega\rho\pi}$, to share the same value. Consequently, there are four undetermined parameters left, namely two coupling constants, one cut-off and one bare mass. Once $g_{\rho\pi\pi}$ and $\Lambda_{\rho\pi\pi}$ are fixed, the other parameters at μ_π can also be determined from the decay width of $\omega \rightarrow 3\pi$ and the P -wave phase shifts of $\pi\pi \rightarrow \pi\pi$ at the physical pion mass μ_π .

The detailed procedure for parameter determination is presented in Appendix B. Here, we simply summarize the preferred values: $g_{\rho\pi\pi} = 7.07$ (6.75) and $\Lambda_{\omega\rho\pi} = \Lambda_{\rho\pi\pi} = 900$ (980) MeV for $N_f = 2 + 1$ ($N_f = 2$)

and $g_{\omega\rho\pi} = 18/\text{GeV}$ for either N_f . It is worth mentioning that our value of $g_{\omega\rho\pi}$ is similar to that used in Ref. [51], 16/GeV. Additionally, $g_{\rho\pi\pi}$ and $\Lambda_{\omega\rho\pi}$ are slightly shifted compared to those found using scheme B, because of the introduction of the $\omega\pi$ channel. We then proceed to minimize the total χ^2 by fitting the value of m_ρ^{B} for each pion mass.

The fitted spectra as functions of the spatial extent, L , for scheme C are shown as black dotted lines in the figures of Appendix D, which illustrates only minor discrepancies from the orange dot-dashed lines found using scheme B, as expected. The fitted values of m_ρ^{B} are presented in the lower portion of Fig. 3 and are tabulated in the columns for scheme C in Table III. The preferred values of m_ρ^{B} are about 50 MeV higher than found in scheme B because of the additional self-energy term, $\Sigma_{\omega\pi}$, as defined in Eq. (17).

Even after including the effect of the $\omega\pi$ coupled channel, the m_π -dependence of m_ρ^{B} shown in Fig.3 is still scattered. It becomes apparent that the bare masses extracted from different lattice groups do not permit a consistent interpretation, which indicates the presence of intrinsic systematic differences between the lattice spectra provided by different collaborations. Such discrepancies

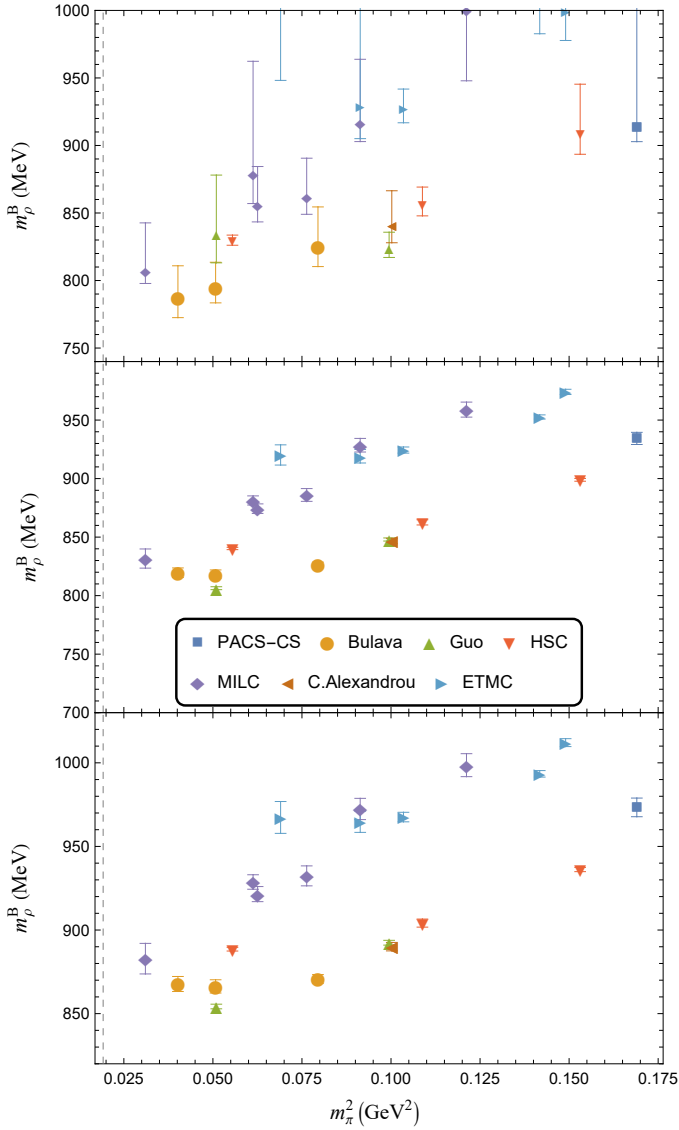


FIG. 3. m_π -dependence of m_ρ^B in schemes A, B and C from top to bottom. The dashed gray vertical line indicates the physical m_π value.

lead us to consider the following issues that may influence the lattice results presented. These include:

- Different residual lattice artefacts due to the different gauge and fermion actions considered.
- Varied scale-setting schemes employed by different collaborations.
- Different methods used to extract the finite volume spectra.

In the absence of systematic errors, the results provided by different collaborations should be consistent with each other after finite volume and lattice spacing artefacts are taken into account. Our HEFT approach enables one to

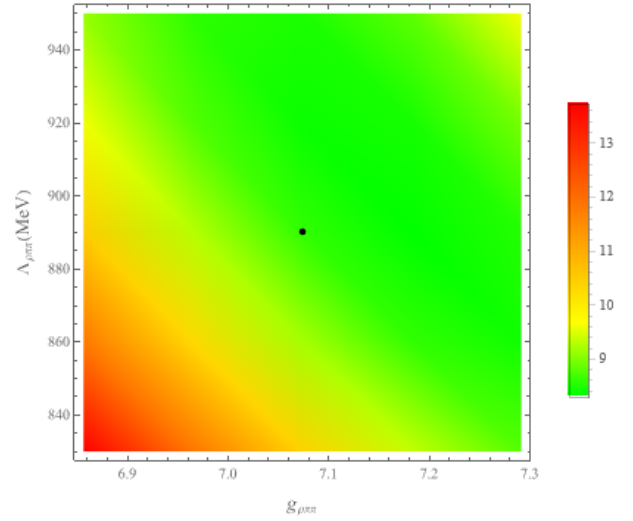


FIG. 4. Distribution of $\sum_{m_\pi \in S} \hat{\chi}^2(m_\pi)$ for scheme B using fixed values of $(g_{\rho\pi\pi}$ and $\Lambda_{\rho\pi\pi})$, where $S = \{301, 302, 315, 316, 322\}$. Using the black point marked in the green region ensures that $\hat{\chi}^2(m_\pi) \lesssim 2$ is satisfied for each value of $m_\pi \in S$.

account for the finite volume of the lattice, several values of the pion mass, as well as lattice spacing artefacts, all within a single formalism. As such, this is the first examination of the self consistency of world lattice QCD results for $\pi\pi$ scattering in ρ meson channel.

D. Extrapolation in m_π

In the last section, we present the outcomes of our fitting approach applied to the finite volume spectra provided by various collaborations for a wide range of values of m_π . With these results, we now investigate the m_π -dependence of the properties of the ρ meson and extrapolate them into the physical region. In scheme A, our investigations reveal that both $g_{\rho\pi\pi}$ and $\Lambda_{\rho\pi\pi}$ display little variation as m_π varies. In the spirit of chiral effective field theory, the couplings and regulator parameters are held fixed. Thus, we could concentrate on the m_π -dependence of the bare ρ mass, m_ρ^B , using Eq. (40). It is possible to extrapolate the fitting results of m_ρ^B in schemes B and C, but not in scheme A, since there the values of m_ρ^B are correlated with $g_{\rho\pi\pi}$ and $\Lambda_{\rho\pi\pi}$.

In principle, it is natural to consider putting all the values of $m_\rho^B(m_\pi)$ together and performing a global fit to make full use of the lattice data. However, from the two lower figures in Fig. 3, it is hard to extract useful information, since the data show large inconsistent variations. The possible reasons have been discussed in the previous section.

For example, with reference to the discussion about the lattice spacing effect in Eq. (41), the coefficient ξ are different for each LQCD group in principle. To confirm this, we applied Eq. (41) with a single value of ξ and

TABLE IV. Extrapolation results are summarized for schemes B and C. For each collaboration, the results of B and C are given in the first and second row, respectively. The second and third column present the coefficient c_0 and c_1 defined in Eq.(40). The fourth column presents the extrapolated m_ρ^B at the physical pion mass. The fifth column presents the pole mass, defined by Eq.(20).

COLLAB.	$c_0(\text{MeV})$	$c_1(\text{GeV}^{-1})$	$m_\rho^B(\mu_\pi)$	$m_\rho^P(\mu_\pi)$
Bulava	809.8(7.0)	0.21(0.11)	814.0(5.0)	765.0(6.0)
	862.3(7.6)	0.11(0.12)	864.0(6.0)	765.0(6.0)
MILC	788.0(7.3)	1.45(0.10)	816.0(6.0)	768.0(6.0)
	843.3(7.95)	1.32(0.11)	869.0(6.0)	769.0(6.0)
HSC	806.7(1.71)	0.60(0.02)	818.2(1.4)	770.6(1.7)
	861.3(1.9)	0.49(0.02)	870.7(1.6)	771.3(1.7)
ETMC	838.9(7.7)	0.85(0.06)	855.0(7.0)	814.0(8.0)
	892.5(8.3)	0.75(0.06)	907.0(7.0)	809.0(7.0)
Guo	762.2(2.9)	0.86(0.04)	778.8(2.3)	719.3(2.6)
	813.8(3.2)	0.79(0.04)	829.0(2.5)	719.0(2.6)

found a large χ^2 .

Also, there is a huge difference between the values of observables calculated using the parameters extrapolated to physical m_π and those measured in experiments. This suggests that we should make the extrapolation of the data to the physical point collaboration by collaboration.

Because for each group, there are only a limited number of values of m_π and the lattice spacing does not change a lot, the lattice spacing term can be absorbed and we just use Eq. (40) to perform the extrapolations. Furthermore, we have two free parameters in Eq. (40), thus only the data of collaborations having no less than two m_π points are analyzed. The fitting and extrapolation results are shown in Fig. 5 and Table IV.

As shown in Fig. 5, there are five collaborations having no less than two different m_π points. For each collaboration, the points show a good linear relation between m_ρ^B and m_π^2 , whether the $\omega\pi$ loop is included or not. The only notable exception is one point with a large uncertainty from ETMC. With c_0 and c_1 determined, we can obtain the bare mass of the ρ at the physical pion mass. Subsequently, we can get m_ρ^P by solving Eq. (20). The results are listed in the last column of Table IV.

For MILC, HSC and Bulava *et al.*, even though their values of c_0 and c_1 are quite different, the extrapolated m_ρ^P all agree with the experimental value. However, for ETMC and Guo *et al.*, they are about 30 MeV higher and 50 MeV lower compared to the experimental value, respectively. The relatively high m_ρ^P obtained by ETMC is not so surprising, since in their previous work [31] a higher value of m_ρ compared to the others was also reported. The lower m_ρ^P extracted from Guo *et al.* also agrees with their own result, presented in Ref. [32], which possibly results from using $N_f = 2$. Clearly, the physical

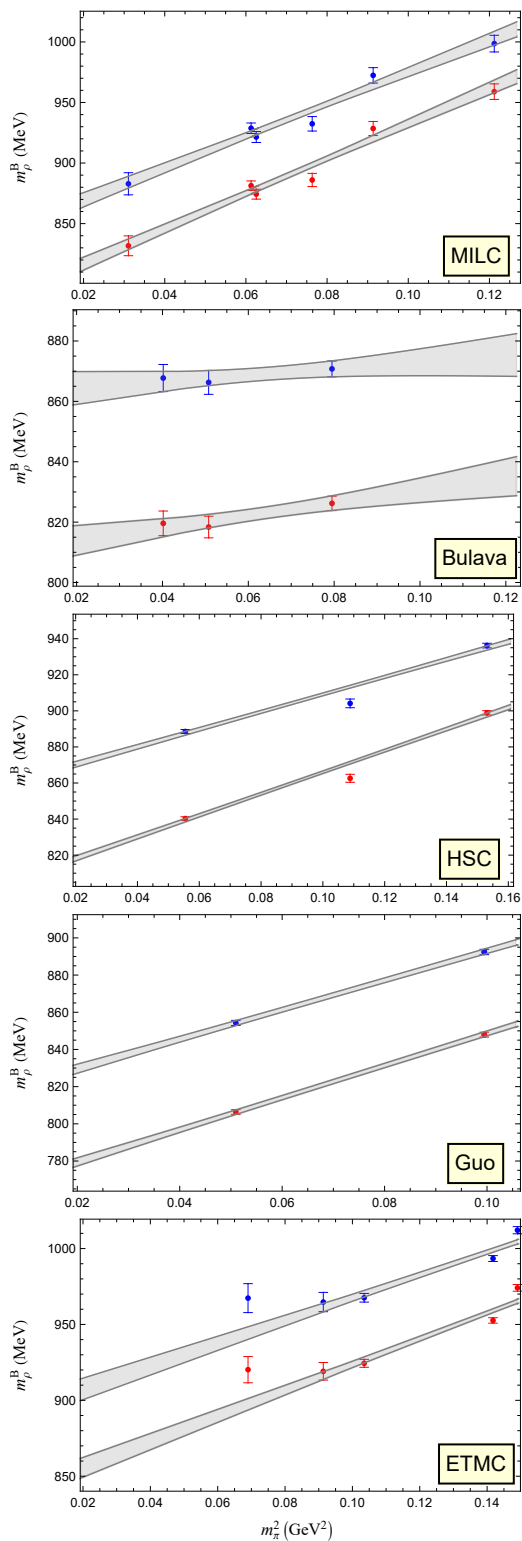


FIG. 5. m_π -dependence and extrapolation of m_ρ^B for each collaboration. Red and blue points indicate the fitting results of m_ρ^B in schemes B and C, respectively. Gray bands represent the quadratic function $m_\rho^B = c_0 + c_1 m_\pi^2$ with uncertainty, where c_0 and c_1 for both schemes are given in Table IV. For convenience the lower bound of the m_π^2 -axis is set as the physical value μ_π^2 .

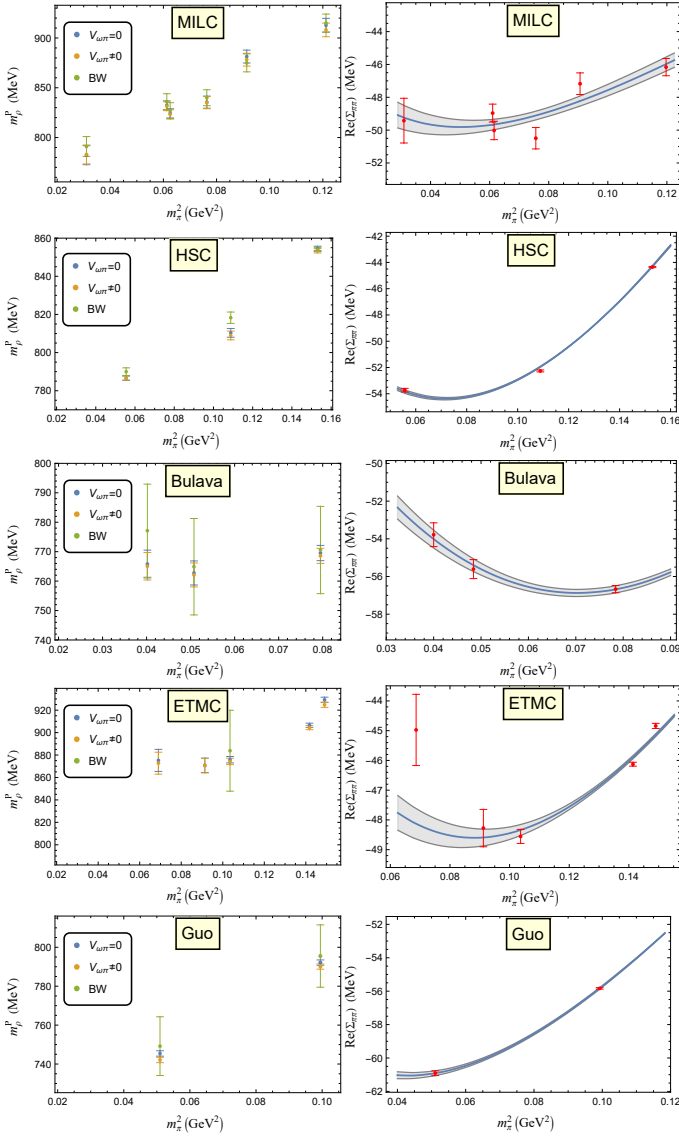


FIG. 6. m_π -dependence of m_ρ^p and the real part of the self-energy $\Sigma_{\pi\pi}$. Left column: m_ρ^p defined by Eq.(20) using parameters for schemes B and C, and m_ρ obtained from the Breit-Wigner parameterization of the phase shift provided in each paper. Right column: real part of the self-energy $\Sigma_{\pi\pi}$. Blue lines with gray bands represent the $\text{Re}\Sigma_{\pi\pi} = m_\rho^p(m_\rho^B) - m_\rho^B$ as in Eq.(39) using $m_\rho^B = c_0 + c_1 m_\pi^2$ with c_0 and c_1 being the extrapolation coefficients for scheme B presented in Table IV. Red points also represent $\text{Re}\Sigma_{\pi\pi}$ but using m_ρ^B from fitting results of scheme B presented in Table III.

ρ masses obtained here all indicate the consistency between our method and previous work, while in addition we provide detailed information on the m_π -dependence of m_ρ^B .

E. Discussion and Exploration

In this section, we make some remarks concerning the numerical results. In scheme A, we first found that the coupling constants $g_{\rho\pi\pi}$ and cut-off $\Lambda_{\rho\pi\pi}$ are both weakly dependent on m_π . This conclusion supports our previous study of the baryon resonances, $\Lambda(1405)$, $N^*(1535)$ and $N^*(1440)$ (Roper), where we only considered the m_π dependence of the masses of various hadrons but not the couplings and cut-off. Furthermore, the large uncertainty found for the cut-off is also acceptable, because in principle the physical observables should not be so sensitive to it.

In Eq. (38), there are many nonlinear terms in m_π^2 , arising from the self-energy part. In the right column of Fig. 6, we show the value of the $\text{Re}\Sigma_{\pi\pi}$ at the pole position as a function of m_π^2 . Given m_ρ^B , $\text{Re}\Sigma_{\pi\pi}$ is calculated by $m_\rho^p - m_\rho^B$ as in Eq. (39), where m_ρ^p is obtained from Eq. (20). Scalars in the figure are calculated by using the values of m_ρ^B from the fitting results of scheme B presented in Table III, while the lines with error bands use $m_\rho^B = c_0 + c_1 m_\pi^2$, with c_0 and c_1 being the coefficients for scheme B presented in Table IV.

Clearly both these scalars and lines in Fig. 6 exhibit a nonlinear behavior. However, the difference of $\text{Re}\Sigma_{\pi\pi}$ at different m_π are just around 10 MeV when m_π varies over the range 140 to 400 MeV. Therefore, there will also be an approximately linear relation between m_ρ^p and m_π^2 , as shown in the left column of Fig. 6, where the Breit-Wigner masses provided by the three collaborations are also shown. This is the reason why the Breit-Wigner ρ mass could be described well by a linear function of m_π^2 in Ref. [33].

Things are similar even when the $\omega\pi$ channel is introduced. From Table IV one can see that m_ρ^p is nearly unchanged while m_ρ^B changes a lot when $V_{\omega\pi}$ turns on. Nonetheless, m_ρ^B still exhibits a linear relation to m_π^2 as shown in Fig. 5, where the two lines are almost parallel for each LQCD group. Also, it is apparent that the contribution from the $\omega\pi$ loop only makes a significant change in the value of c_0 , but just slightly modifies the slope, c_1 . These facts suggest that $\text{Re}\Sigma_{\omega\pi}$ is also weakly dependent on m_π and its effect can be effectively absorbed into c_0 .

In summary, the slow variation of the contributions from $\pi\pi$ and $\omega\pi$ loops significantly affects c_0 , while only slightly influencing the slope, c_1 . Therefore, it makes little sense to talk about m_ρ^B solely based on experimental results, as the fitted m_ρ^B strongly depends on how the hadronic loops are estimated. It is the slope c_1 that contains more useful, less model dependent, physical information concerning the structure of the ρ meson, which can only be extracted from the LQCD data at unphysical m_π . Furthermore, in principle, on the theoretical side the slope c_1 can be calculated at the quark-level in various models. Thus, with the help of c_1 the relevant models could be distinguished. This is quite a good example of the idea that the data extracted at unphysical values of

TABLE V. Composition of eigenstates $|\psi\rangle$ of some energy levels from HSC(2015). In the first column, $|\psi\rangle$ is labelled by (\mathbf{n}^2, Γ) , as it is the eigenstate that has the largest ρ_B component among those whose energies are extracted by the operators in representation Γ and with total momentum $\mathbf{P}^2 = (\frac{2\pi}{L})^2 \mathbf{n}^2$, as shown in Fig. 16. In the subsequent column we present the composition of $|\psi\rangle$, i.e. $|\langle\phi|\psi\rangle|^2$ with $|\phi\rangle = |\rho_B\rangle, |\pi\pi\rangle$ for $V_{\omega\pi} = 0$ and also $|\omega\pi\rangle$ for $V_{\omega\pi} \neq 0$.

(\mathbf{n}^2, Γ)	$V_{\omega\pi} = 0$		$V_{\omega\pi} \neq 0$		
	ρ_B	$\pi\pi$	ρ_B	$\pi\pi$	$\omega\pi$
$(1, A_1)$	0.7365	0.2635	0.6966	0.2664	0.0370
$(2, A_1)$	0.7963	0.2037	0.7537	0.2028	0.0434
$(3, A_1)$	0.7701	0.2299	0.7295	0.2241	0.0464
$(4, A_1)$	0.7432	0.2568	0.7093	0.2503	0.0404
$(3, E)$	0.6514	0.3486	0.6171	0.3394	0.0434

m_π are able to provide us with additional information concerning the structure of hadrons.

The linear relation between m_ρ^B and m_π^2 is consistent with the assumption that $|\rho_B\rangle$ is a pure $q\bar{q}$ state. Additionally, the contribution from hadron loops to m_ρ^P accounts for only approximately 20% of the total mass for the optimal value of the regulator parameter. Consequently, we can also conclude that the bare ρ plays the most important role in the structure of the observed ρ meson. To confirm this, we pick out several eigenstates whose energy is close to the physical ρ mass and look at their composition, a feature which is characteristic of HEFT. The eigenstates of the FVH are the counterpart in the finite volume of continuous scattering states in the infinite volume [43]. Therefore, obviously, it is expected that the eigenstate whose energy is closest to the resonance region is the counterpart of the ρ . For illustration, we pick five eigenstates from the spectrum generated by HSC(2015) with $m_\pi = 236$ MeV and calculate the probabilities of the bare state, $\pi\pi$ and $\omega\pi$ components. The results are presented in Table V. It is found that the component ρ_B has a probability around 75%. That is, it is definitely dominant.

With the parameters listed in Table III, we can predict the $\pi\pi \rightarrow \pi\pi$ P -wave phase shift at unphysical masses. Here we focus on the three collaborations whose values of m_ρ^P at the physical m_π agree with the experimental value. In Fig. 7, we show the phase shifts calculated for four different values of m_π . In the first row, at the physical point, the phase shifts of the three collaborations are nearly the same. This is expected since their values of m_ρ^B at physical m_π are consistent. They are in good agreement with the experimental data, except for the region away from resonance, where the $\pi\pi - \pi\pi$ t/u -channel interaction may not be negligible.

In other rows we predict the phase shifts of the three collaborations at three unphysical values of m_π . Since the values of c_0 and c_1 obtained by analysis of the data

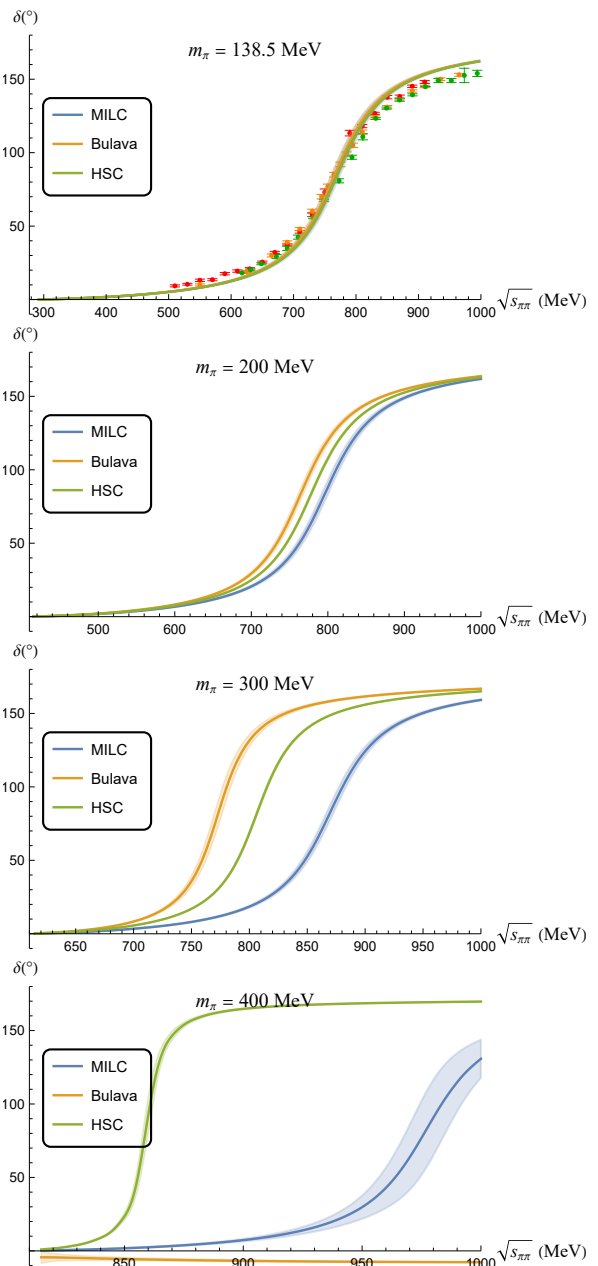


FIG. 7. Phase shift calculated by Eq. (19) using the parameters $g_{\omega\rho\pi} = 0$, $g_{\rho\pi\pi} = 7.07$, $\Lambda_{\rho\pi\pi} = 890$ MeV and $m_\rho = c_0 + c_1 m_\pi^2$ with c_0 and c_1 being the extrapolation coefficients for scheme B given in Table IV. The points in the first figure are experimental values from Ref. [71–73]. The line for Bulava at $m_\pi = 400$ MeV denotes a $\pi\pi$ bound state.

from these three collaborations are very different, their phase shifts are not consistent. Especially, for $m_\pi = 400$ MeV, we predict that the typical line shape would disappear in the phase shifts of $\pi\pi$ scattering for Bulava *et al.*, since it would be a bound state of $\pi\pi$.

The most serious problem found in this work is that the two coefficients, c_0 and c_1 , differ a lot for different LQCD groups. This unexpected variation arises from dif-

ferences in the lattice QCD simulations, the interpolating fields considered in constructing correlation matrices, the analysis methods applied to the correlation matrices and finally the scale-setting schemes.

The use of different $\mathcal{O}(a)$ -improved actions gives rise to different $\mathcal{O}(a^2)$ errors such that the coefficient of a^2 differs for each set of lattice QCD results. It will be important to have two or more different lattice spacings available in high-quality sets to enable a determination and elimination of this lattice artefact.

State isolation is key to measuring the subtle shifts of the finite-volume energies from their non-interacting energies, vital to measuring a phase shift. In obtaining consistency across lattice collaborations, modern projected correlator methods should be adopted to reduce excited state contamination in the extracted energy eigenvalues. Moreover, all nonlocal two particle momentum-projected interpolating fields participating in the resonance region need to be considered and mixed with the single particle operators to ensure multiple eigenstates are not participating in the state-projected correlation functions of the correlation matrix. In the present case, single particle ρ interpolations are to be mixed, not only with $\pi\pi$ correlations, but also with $\pi\omega$ correlators. Indeed, Fig. 1 and the figures in Appendix.D, illustrating the fits of HEFT to contemporary lattice QCD results, raise concerns about multi-state contamination in the analysis.

Finally, the choice of scale setting scheme is of vital importance when attempting to describe QCD properties away from the physical point. While all schemes are designed to extrapolate to the physical point, the manner in which they move away from the physical point is different. The Sommer scale is designed to be physical. Maintaining physics at the scale relevant to the charmonium spectrum, it naturally includes changes in the renormalization of the strong coupling constant due to changes in the sea quark masses. However, other schemes where the quark mass has no effect on the coupling constant are possible, provided the only goal is to get to the physical point. In light of the plethora of scale setting schemes currently proposed, we encourage the consideration of how well a proposed scheme is suited to learning the properties of QCD in a universe with different quark masses.

IV. SUMMARY AND OUTLOOK

In this work, we collected finite volume spectra for the $I = \ell = 1$ $\pi\pi$ sector provided by LQCD collaborations over the past decade. These spectra were fit in a consistent manner within the framework of Hamiltonian Effective field theory. The basic states included in the Hamiltonian were a bare ρ state and the $\pi\pi$ and $\omega\pi$ coupled channels. In this framework, we successfully fit the finite volume spectra in the rest frame, moving frame and the elongated box, and complemented this with experimental data for the $\pi\pi \rightarrow \pi\pi$ P -wave phase shifts.

We employed three schemes to fit the energy levels obtained at various pion masses. Through scheme A, we found that $g_{\rho\pi\pi}$ and $\Lambda_{\rho\pi\pi}$ exhibit a weak dependence on m_π . In the following scheme B, we set these two parameters as constant in order to obtain the m_π -dependence of the bare ρ basis state, $m_\rho^B(m_\pi)$. In scheme C, where the $\omega\rho\pi$ vertex was included with additional constraints from experimental data, we again extracted $m_\rho^B(m_\pi)$. Finally, we used the linear relation between m_ρ^B and m_π^2 , as shown in Eq. (38), to perform an extrapolation. Because the relationship between m_ρ^B and m_π^2 was highly dependent on the LQCD group whose data we used, we were unable to fit all m_ρ^B simultaneously, and resorted to extrapolating collaboration by collaboration.

Based upon the extrapolations of data from the five LQCD groups, it was found that for each collaboration, $m_\rho^B(m_\pi)$ could be described well by Eq. (40). This supports the hypothesis that the single-particle bare ρ meson plays an important role in forming a physical peak in the P -wave $\pi\pi$ scattering. The pole mass m_ρ^P defined by Eq. (39) are also calculated. When extrapolated to physical pion mass μ_π , the m_ρ^P for MILC, Bulava *et al.* and HSC agree with the experimental measurements. We can also predict the observables such as the phase shift for each collaboration at some certain unphysical m_π . For each group, the pole mass m_ρ^P and the coefficients c_1 in Eq. (40) were stable with and without the $\omega\pi$ loop contribution, while the bare mass had a shift of around 50 MeV. Unfortunately, from the current LQCD data, the extracted value of c_1 is dependent on the lattice collaboration whose data is used. This indicates the important discrepancies in the results of today's lattice QCD calculation among different collaborations due to the possible reasons discussed previously. In the future it would obviously be ideal to have lattice data for the ρ meson at different pion masses with all systematic effects carefully controlled in order to resolve the m_π -dependence of the ρ meson.

ACKNOWLEDGMENTS

We acknowledge useful discussions and valuable comments from Xu Feng, Feng-Kun Guo, Chuan Liu, Li-uming Liu, Guang-Juan Wang, Mao-Jun Yan, Yi-Bo Yang, Zhi Yang, Bing-Song Zou. This work was partly supported by the National Natural Science Foundation of China (NSFC) under Grants Nos. 12175239 and 12221005 (J.J.W), and by the National Key R&D Program of China under Contract No. 2020YFA0406400 (J.J.W), and by the Chinese Academy of Sciences under Grant No. YSBR-101 (J.J.W). This research was also undertaken with assistance of resources from the National Computational Infrastructure(NCI), provided through the National Computational Merit Allocation Scheme. This work was supported by the Australian Research Council through Discovery Projects DP190102215 and DP210103706 (DBL) and DP230101791 (AWT). Y.

L. is supported by the Excellence Hub project "Unraveling the 3D parton structure of the nucleon with lattice QCD (3D-nucleon)" id EXCELLENCE/0421/0043 co-financed by the European Regional Development Fund and the Republic of Cyprus through the Research and Innovation Foundation. Y. L. further acknowledges computing time granted on Piz Daint at Centro Svizzero di

Calcolo Scientifico (CSCS) via the project with id s1174, JUWELS Booster at the Jülich Supercomputing Centre (JSC) via the project with id pines, and Cyclone at the Cyprus institute (CYI) via the project with ids P061, P146 and pro22a10951.

-
- [1] S. Capstick and W. Roberts, Quark models of baryon masses and decays, *Prog. Part. Nucl. Phys.* **45**, S241 (2000), arXiv:nucl-th/0008028.
- [2] T. A. DeGrand, R. L. Jaffe, K. Johnson, and J. E. Kiskis, Masses and Other Parameters of the Light Hadrons, *Phys. Rev. D* **12**, 2060 (1975).
- [3] S. Theberge, A. W. Thomas, and G. A. Miller, The Cloudy Bag Model. 1. The (3,3) Resonance, *Phys. Rev. D* **22**, 2838 (1980), [Erratum: *Phys.Rev.D* 23, 2106 (1981)].
- [4] A. W. Thomas, S. Theberge, and G. A. Miller, The Cloudy Bag Model of the Nucleon, *Phys. Rev. D* **24**, 216 (1981).
- [5] C. D. Roberts and A. G. Williams, Dyson-Schwinger equations and their application to hadronic physics, *Prog. Part. Nucl. Phys.* **33**, 477 (1994), arXiv:hep-ph/9403224.
- [6] F.-K. Guo, C. Hanhart, U.-G. Meißner, Q. Wang, Q. Zhao, and B.-S. Zou, Hadronic molecules, *Rev. Mod. Phys.* **90**, 015004 (2018), [Erratum: *Rev.Mod.Phys.* 94, 029901 (2022)], arXiv:1705.00141 [hep-ph].
- [7] C. A. Meyer and E. S. Swanson, Hybrid Mesons, *Prog. Part. Nucl. Phys.* **82**, 21 (2015), arXiv:1502.07276 [hep-ph].
- [8] A. W. Thomas, Chiral extrapolation of hadronic observables, *Nucl. Phys. B Proc. Suppl.* **119**, 50 (2003), arXiv:hep-lat/0208023.
- [9] M. Luscher, Two particle states on a torus and their relation to the scattering matrix, *Nucl. Phys. B* **354**, 531 (1991).
- [10] C. h. Kim, C. T. Sachrajda, and S. R. Sharpe, Finite-volume effects for two-hadron states in moving frames, *Nucl. Phys. B* **727**, 218 (2005), arXiv:hep-lat/0507006.
- [11] M. T. Hansen and S. R. Sharpe, Multiple-channel generalization of Lellouch-Luscher formula, *Phys. Rev. D* **86**, 016007 (2012), arXiv:1204.0826 [hep-lat].
- [12] S. He, X. Feng, and C. Liu, Two particle states and the S-matrix elements in multi-channel scattering, *JHEP* **07**, 011, arXiv:hep-lat/0504019.
- [13] K. Rummukainen and S. A. Gottlieb, Resonance scattering phase shifts on a nonrest frame lattice, *Nucl. Phys. B* **450**, 397 (1995), arXiv:hep-lat/9503028.
- [14] M. Gockeler, R. Horsley, M. Lage, U. G. Meissner, P. E. L. Rakow, A. Rusetsky, G. Schierholz, and J. M. Zanotti, Scattering phases for meson and baryon resonances on general moving-frame lattices, *Phys. Rev. D* **86**, 094513 (2012), arXiv:1206.4141 [hep-lat].
- [15] K. G. Wilson, Confinement of Quarks, *Phys. Rev. D* **10**, 2445 (1974).
- [16] Y. Aoki *et al.* (Flavour Lattice Averaging Group (FLAG)), FLAG Review 2021, *Eur. Phys. J. C* **82**, 869 (2022), arXiv:2111.09849 [hep-lat].
- [17] R. A. Briceno, J. J. Dudek, and R. D. Young, Scattering processes and resonances from lattice QCD, *Rev. Mod. Phys.* **90**, 025001 (2018), arXiv:1706.06223 [hep-lat].
- [18] R. L. Workman *et al.* (Particle Data Group), Review of Particle Physics, *PTEP* **2022**, 083C01 (2022).
- [19] F. Aceti and E. Oset, Wave functions of composite hadron states and relationship to couplings of scattering amplitudes for general partial waves, *Phys. Rev. D* **86**, 014012 (2012), arXiv:1202.4607 [hep-ph].
- [20] R. L. Jaffe, Ordinary and extraordinary hadrons, *AIP Conf. Proc.* **964**, 1 (2007), arXiv:hep-ph/0701038.
- [21] J. R. Pelaez, On the Nature of light scalar mesons from their large N(c) behavior, *Phys. Rev. Lett.* **92**, 102001 (2004), arXiv:hep-ph/0309292.
- [22] J. R. Pelaez and G. Rios, Nature of the f0(600) from its N(c) dependence at two loops in unitarized Chiral Perturbation Theory, *Phys. Rev. Lett.* **97**, 242002 (2006), arXiv:hep-ph/0610397.
- [23] C. B. Lang, D. Mohler, S. Prelovsek, and M. Vidmar, Coupled channel analysis of the rho meson decay in lattice QCD, *Phys. Rev. D* **84**, 054503 (2011), [Erratum: *Phys.Rev.D* 89, 059903 (2014)], arXiv:1105.5636 [hep-lat].
- [24] S. Aoki *et al.* (CS), ρ Meson Decay in 2+1 Flavor Lattice QCD, *Phys. Rev. D* **84**, 094505 (2011), arXiv:1106.5365 [hep-lat].
- [25] G. S. Bali, S. Collins, A. Cox, G. Donald, M. Göckeler, C. B. Lang, and A. Schäfer (RQCD), ρ and K^* resonances on the lattice at nearly physical quark masses and $N_f = 2$, *Phys. Rev. D* **93**, 054509 (2016), arXiv:1512.08678 [hep-lat].
- [26] D. J. Wilson, R. A. Briceno, J. J. Dudek, R. G. Edwards, and C. E. Thomas, Coupled $\pi\pi$, $K\bar{K}$ scattering in P -wave and the ρ resonance from lattice QCD, *Phys. Rev. D* **92**, 094502 (2015), arXiv:1507.02599 [hep-ph].
- [27] J. J. Dudek, R. G. Edwards, and C. E. Thomas (Hadron Spectrum), Energy dependence of the ρ resonance in $\pi\pi$ elastic scattering from lattice QCD, *Phys. Rev. D* **87**, 034505 (2013), [Erratum: *Phys.Rev.D* 90, 099902 (2014)], arXiv:1212.0830 [hep-ph].
- [28] M. Werner *et al.* (Extended Twisted Mass), Hadron-Hadron Interactions from $N_f = 2 + 1 + 1$ Lattice QCD: The ρ -resonance, *Eur. Phys. J. A* **56**, 61 (2020), arXiv:1907.01237 [hep-lat].
- [29] C. Alexandrou, L. Leskovec, S. Meinel, J. Negele, S. Paul, M. Petschlies, A. Pochinsky, G. Rendon, and S. Syritsyn, P -wave $\pi\pi$ scattering and the ρ resonance from lattice QCD, *Phys. Rev. D* **96**, 034525 (2017), arXiv:1704.05439 [hep-lat].
- [30] C. Pelissier and A. Alexandru, Resonance parameters of the rho-meson from asymmetrical lattices, *Phys. Rev. D* **87**, 014503 (2013), arXiv:1211.0092 [hep-lat].
- [31] X. Feng, K. Jansen, and D. B. Renner, Resonance Param-

- eters of the rho-Meson from Lattice QCD, Phys. Rev. D **83**, 094505 (2011), arXiv:1011.5288 [hep-lat].
- [32] D. Guo, A. Alexandru, R. Molina, and M. Döring, Rho resonance parameters from lattice QCD, Phys. Rev. D **94**, 034501 (2016), arXiv:1605.03993 [hep-lat].
- [33] Z. Fu and L. Wang, Studying the ρ resonance parameters with staggered fermions, Phys. Rev. D **94**, 034505 (2016), arXiv:1608.07478 [hep-lat].
- [34] C. Andersen, J. Bulava, B. Hörz, and C. Morningstar, The $I = 1$ pion-pion scattering amplitude and timelike pion form factor from $N_f = 2 + 1$ lattice QCD, Nucl. Phys. B **939**, 145 (2019), arXiv:1808.05007 [hep-lat].
- [35] M. Fischer, B. Kostrzewa, M. Mai, M. Petschlies, F. Pittler, M. Ueding, C. Urbach, and M. Werner (Extended Twisted Mass, ETM), The ρ -resonance from $N_f = 2$ lattice QCD including the physical pion mass, Phys. Lett. B **819**, 136449 (2021), arXiv:2006.13805 [hep-lat].
- [36] A. Rodas, J. J. Dudek, and R. G. Edwards, The quark mass dependence of $\pi\pi$ scattering in isospin 0, 1 and 2 from lattice QCD, (2023), arXiv:2303.10701 [hep-lat].
- [37] B. Hu, R. Molina, M. Döring, M. Mai, and A. Alexandru, Chiral extrapolations of the $\rho(770)$ meson in $N_f = 2 + 1$ lattice QCD simulations, Phys. Rev. D **96**, 034520 (2017), arXiv:1704.06248 [hep-lat].
- [38] B. Hu, R. Molina, M. Döring, and A. Alexandru, Two-flavor Simulations of the $\rho(770)$ and the Role of the $K\bar{K}$ Channel, Phys. Rev. Lett. **117**, 122001 (2016), arXiv:1605.04823 [hep-lat].
- [39] M. Doring, J. Haidenbauer, U.-G. Meissner, and A. Rusetsky, Dynamical coupled-channel approaches on a momentum lattice, Eur. Phys. J. A **47**, 163 (2011), arXiv:1108.0676 [hep-lat].
- [40] M. Doring, U. G. Meissner, E. Oset, and A. Rusetsky, Scalar mesons moving in a finite volume and the role of partial wave mixing, Eur. Phys. J. A **48**, 114 (2012), arXiv:1205.4838 [hep-lat].
- [41] J.-J. Wu, T. S. H. Lee, A. W. Thomas, and R. D. Young, Finite-volume Hamiltonian method for coupled-channels interactions in lattice QCD, Phys. Rev. C **90**, 055206 (2014), arXiv:1402.4868 [hep-lat].
- [42] Z.-W. Liu, W. Kamleh, D. B. Leinweber, F. M. Stokes, A. W. Thomas, and J.-J. Wu, Hamiltonian effective field theory study of the $N^*(1440)$ resonance in lattice QCD, Phys. Rev. D **95**, 034034 (2017), arXiv:1607.04536 [nucl-th].
- [43] J.-j. Wu, D. B. Leinweber, Z.-w. Liu, and A. W. Thomas, Structure of the Roper Resonance from Lattice QCD Constraints, Phys. Rev. D **97**, 094509 (2018), arXiv:1703.10715 [nucl-th].
- [44] Z.-W. Liu, J. M. M. Hall, D. B. Leinweber, A. W. Thomas, and J.-J. Wu, Structure of the $\Lambda(1405)$ from Hamiltonian effective field theory, Phys. Rev. D **95**, 014506 (2017), arXiv:1607.05856 [nucl-th].
- [45] Z.-W. Liu, W. Kamleh, D. B. Leinweber, F. M. Stokes, A. W. Thomas, and J.-J. Wu, Hamiltonian effective field theory study of the $N^*(1535)$ resonance in lattice QCD, Phys. Rev. Lett. **116**, 082004 (2016), arXiv:1512.00140 [hep-lat].
- [46] Z. Yang, G.-J. Wang, J.-J. Wu, M. Oka, and S.-L. Zhu, Novel Coupled Channel Framework Connecting the Quark Model and Lattice QCD for the Near-threshold Ds States, Phys. Rev. Lett. **128**, 112001 (2022), arXiv:2107.04860 [hep-ph].
- [47] Y. Li, J.-J. Wu, C. D. Abell, D. B. Leinweber, and A. W. Thomas, Partial Wave Mixing in Hamiltonian Effective Field Theory, Phys. Rev. D **101**, 114501 (2020), arXiv:1910.04973 [hep-lat].
- [48] Y. Li, J.-j. Wu, D. B. Leinweber, and A. W. Thomas, Hamiltonian effective field theory in elongated or moving finite volume, Phys. Rev. D **103**, 094518 (2021), arXiv:2103.12260 [hep-lat].
- [49] S. Weinberg, *The Quantum theory of fields. Vol. 1: Foundations* (Cambridge University Press, 2005).
- [50] A. Matsuyama, T. Sato, and T. S. H. Lee, Dynamical coupled-channel model of meson production reactions in the nucleon resonance region, Phys. Rept. **439**, 193 (2007), arXiv:nucl-th/0608051.
- [51] D. B. Leinweber, A. W. Thomas, K. Tsushima, and S. V. Wright, Chiral behavior of the rho meson in lattice QCD, Phys. Rev. D **64**, 094502 (2001), arXiv:hep-lat/0104013.
- [52] J.-J. Wu, T. S. H. Lee, and B. S. Zou, Nucleon Resonances with Hidden Charm in Coupled-Channel Models, Phys. Rev. C **85**, 044002 (2012), arXiv:1202.1036 [nucl-th].
- [53] V. Bernard, M. Lage, U.-G. Meissner, and A. Rusetsky, Resonance properties from the finite-volume energy spectrum, JHEP **08**, 024, arXiv:0806.4495 [hep-lat].
- [54] C. R. Allton, W. Armour, D. B. Leinweber, A. W. Thomas, and R. D. Young, Chiral and continuum extrapolation of partially-quenched lattice results, Phys. Lett. B **628**, 125 (2005), arXiv:hep-lat/0504022.
- [55] P. C. Bruns and U.-G. Meissner, Infrared regularization for spin-1 fields, Eur. Phys. J. C **40**, 97 (2005), arXiv:hep-ph/0411223.
- [56] W. Armour, C. R. Allton, D. B. Leinweber, A. W. Thomas, and R. D. Young, Unified chiral analysis of the vector meson spectrum from lattice QCD, J. Phys. G **32**, 971 (2006), arXiv:hep-lat/0510078.
- [57] H.-X. Chen and E. Oset, $\pi\pi$ interaction in the ρ channel in finite volume, Phys. Rev. D **87**, 016014 (2013), arXiv:1202.2787 [hep-lat].
- [58] R. Molina and J. Ruiz de Elvira, Light- and strange-quark mass dependence of the $\rho(770)$ meson revisited, JHEP **11**, 017, arXiv:2005.13584 [hep-lat].
- [59] M. Niehus, M. Hoferichter, B. Kubis, and J. Ruiz de Elvira, Two-Loop Analysis of the Pion Mass Dependence of the ρ Meson, Phys. Rev. Lett. **126**, 102002 (2021), arXiv:2009.04479 [hep-ph].
- [60] J. M. M. Hall, A. C. P. Hsu, D. B. Leinweber, A. W. Thomas, and R. D. Young, Finite-volume matrix Hamiltonian model for a $\Delta \rightarrow N\pi$ system, Phys. Rev. D **87**, 094510 (2013), arXiv:1303.4157 [hep-lat].
- [61] C. D. Abell, D. B. Leinweber, A. W. Thomas, and J.-J. Wu, Regularization in nonperturbative extensions of effective field theory, Phys. Rev. D **106**, 034506 (2022), arXiv:2110.14113 [hep-lat].
- [62] C. Morningstar, J. Bulava, A. D. Hanlon, B. Hörz, D. Mohler, A. Nicholson, S. Skinner, and A. Walker-Loud, Progress on Meson-Baryon Scattering, PoS **LAT-TICE2021**, 170 (2022), arXiv:2111.07755 [hep-lat].
- [63] C. B. Lang, L. Leskovec, M. Padmanath, and S. Prelovsek, Pion-nucleon scattering in the Roper channel from lattice QCD, Phys. Rev. D **95**, 014510 (2017), arXiv:1610.01422 [hep-lat].
- [64] C. D. Abell, D. B. Leinweber, Z.-W. Liu, A. W. Thomas, and J.-J. Wu, Low-lying odd-parity nucleon resonances as quark-model-like states, Phys. Rev. D **108**, 094519 (2023), arXiv:2306.00337 [hep-lat].

- [65] J. Bulava, A. D. Hanlon, B. Hörz, C. Morningstar, A. Nicholson, F. Romero-López, S. Skinner, P. Vranas, and A. Walker-Loud, Elastic nucleon-pion scattering at $m\pi=200$ MeV from lattice QCD, Nucl. Phys. B **987**, 116105 (2023), arXiv:2208.03867 [hep-lat].
- [66] R. G. Edwards, J. J. Dudek, D. G. Richards, and S. J. Wallace, Excited state baryon spectroscopy from lattice QCD, Phys. Rev. D **84**, 074508 (2011), arXiv:1104.5152 [hep-ph].
- [67] R. G. Edwards, N. Mathur, D. G. Richards, and S. J. Wallace (Hadron Spectrum), Flavor structure of the excited baryon spectra from lattice QCD, Phys. Rev. D **87**, 054506 (2013), arXiv:1212.5236 [hep-ph].
- [68] C. B. Lang and V. Verduci, Scattering in the πN negative parity channel in lattice QCD, Phys. Rev. D **87**, 054502 (2013), arXiv:1212.5055 [hep-lat].
- [69] F. James and M. Roos, Minuit: A System for Function Minimization and Analysis of the Parameter Errors and Correlations, Comput. Phys. Commun. **10**, 343 (1975).
- [70] F. Kleefeld, E. van Beveren, and G. Rupp, The Pionic width of the $\omega(782)$ meson within a well-defined, unitary quantum field theory of (anti-)particles and (anti-)holes, Nucl. Phys. A **694**, 470 (2001), arXiv:hep-ph/0101247.
- [71] S. D. Protopopescu, M. Alston-Garnjost, A. Barbaro-Galtieri, S. M. Flatte, J. H. Friedman, T. A. Lasinski, G. R. Lynch, M. S. Rabin, and F. T. Solmitz, Pi pi Partial Wave Analysis from Reactions $\pi^+ p \rightarrow \pi^+ \pi^- \Delta^{++}$ and $\pi^+ p \rightarrow K^+ K^- \Delta^{++}$ at 7.1-GeV/c, Phys. Rev. D **7**, 1279 (1973).
- [72] P. Estabrooks and A. D. Martin, pi pi Phase Shift Analysis Below the K anti-K Threshold, Nucl. Phys. B **79**, 301 (1974).
- [73] B. Hyams *et al.*, $\pi\pi$ Phase Shift Analysis from 600-MeV to 1900-MeV, Nucl. Phys. B **64**, 134 (1973).
- [74] S. Aoki and T. Doi, Lattice QCD and baryon-baryon interactions: HAL QCD method, Front. in Phys. **8**, 307 (2020), arXiv:2003.10730 [hep-lat].

Appendix A: The formulas for $\mathbf{n} \leftrightarrow \mathbf{k}^*(\mathbf{n})$ and e_n

Here, we will list all cases involved in our present calculation, since the transformation $\mathbf{n} \leftrightarrow \mathbf{k}^*(\mathbf{n})$ and e_n differ from how the momentum is quantized. A summary is given here.

1. If quantized in a cubic box with total momentum $\mathbf{P} = 0$ and length L , then $\mathbf{k}^*(\mathbf{n}) = \frac{2\pi}{L}\mathbf{n}$, and $e_n = n^2$.
2. If quantized in a elongated box with total momentum $\mathbf{P} = 0$, then $\mathbf{k}^*(\mathbf{n}) = \frac{2\pi}{L}(\mathbf{n}_\perp + \frac{1}{\eta}\mathbf{n}_\parallel)$ where $\eta > 1$ denotes the elongation strength, \perp and \parallel denotes the vertical and parallel component to the elongated direction named \mathbf{d} , respectively. Then e_n need two values, n^2 and $|\mathbf{n} \cdot \mathbf{d}|$.
3. If quantized in a cubic box with total momentum $\mathbf{P} \equiv 2\pi\mathbf{d}/L \neq 0$, then $\mathbf{k}^*(\mathbf{n}) = \mathbf{k}^*(\mathbf{k}(\mathbf{n}))$ and $\mathbf{k}(\mathbf{n}) = \frac{2\pi}{L}\mathbf{n}$ where $\mathbf{k}^*(\mathbf{k})$ is the ‘‘Lorentz-like transformation’’ for channel α defined as

$$\mathbf{k}^*(\mathbf{k}) = \mathbf{k}_\perp + \gamma \left(\mathbf{k}_\parallel - \frac{E_{\alpha_1}(\mathbf{k})}{E_{\alpha_1}(\mathbf{k}) + E_{\alpha_2}(\mathbf{P} - \mathbf{k})} \mathbf{P} \right),$$

$$\gamma = \frac{E_{\alpha_1}(\mathbf{k}) + E_{\alpha_2}(\mathbf{P} - \mathbf{k})}{\sqrt{(E_{\alpha_1}(\mathbf{k}) + E_{\alpha_2}(\mathbf{P} - \mathbf{k}))^2 - \mathbf{P}^2}}, \quad (\text{A1})$$

where $\mathbf{k}_\parallel = (\mathbf{k} \cdot \mathbf{P})\mathbf{P}/\mathbf{P}^2$ and $\mathbf{k}_\perp = \mathbf{k} - \mathbf{k}_\parallel$. Correspondingly the Jacobian is

$$\mathbf{J}(\mathbf{k}) = \frac{E_{\alpha_1}(\mathbf{k}) + E_{\alpha_2}(\mathbf{P} - \mathbf{k})}{E_{\alpha_1}(\mathbf{k}) E_{\alpha_2}(\mathbf{P} - \mathbf{k})} \bigg/ \frac{E_{\alpha_1}(\mathbf{k}^*) + E_{\alpha_2}(\mathbf{k}^*)}{E_{\alpha_1}(\mathbf{k}^*) E_{\alpha_2}(\mathbf{k}^*)}. \quad (\text{A2})$$

And the e_n also needs two values, n^2 and $\mathbf{n} \cdot \mathbf{d}$. Furthermore, please note that for the $\pi\pi$ case, the two values are unordered.

4. If quantized in a elongated box with total momentum $\mathbf{P} \neq 0$ and \mathbf{P} is parallel to the elongated direction \mathbf{d} , it is same as the third case above except that $\mathbf{k}(\mathbf{n}) = \frac{2\pi}{L}(\mathbf{n}_\perp + \frac{1}{\eta}\mathbf{n}_\parallel)$. And the e_n are also the same as that in the third case.

Appendix B: Determination of fixed parameters in Scheme C

In this appendix the determination of $g_{\omega\rho\pi}$ and $\Lambda_{\omega\rho\pi}$ are discussed. As mentioned in the main text, besides lattice spectrum the parameters should also be constrained by the decay width $\Gamma_{\omega \rightarrow 3\pi}$ as well as phase shift $\delta_{\pi\pi \rightarrow \pi\pi}^{\ell=1}$ on the experimental side.

The decay channel $\omega \rightarrow 3\pi$ is believed to be dynamically dominated by the $\omega \rightarrow \rho\pi \rightarrow 3\pi$ mechanism. Therefore, the calculation of the decay width would concern $V_{\pi\pi}$ and $V_{\omega\pi}$ defined in Eq.(7) and (8). States in this appendix are normalized as $\langle \mathbf{p} | \mathbf{k} \rangle = (2\pi)^3 2E_p \delta^3(\mathbf{k} - \mathbf{p})$ unless specified other. Let $|p_1^+ p_2^- p_3^0\rangle$ and $T^\lambda(E; p_1, p_2, p_3)$ denote $|\pi^+(\mathbf{p}_1) \pi^-(\mathbf{p}_2) \pi^0(\mathbf{p}_3)\rangle$ and T-matrix element $\langle p_1^+ p_2^- p_3^0 | T(E) | \omega, \lambda \rangle$ with λ being the polarization of the ω , respectively. Then,

$$T^\lambda(E; p_1, p_2, p_3) = \int \frac{d^3\mathbf{q}}{(2\pi)^6 2E_\rho(\mathbf{q}) 2E_\pi(\mathbf{q})} \sum_\sigma T_\sigma^{I=0}(E; p_1 p_2 p_3; \mathbf{q}) \frac{1}{E - E_\rho(\mathbf{q}) - E_\pi(\mathbf{q})} V_{\omega \rightarrow \rho\pi}^{\lambda\sigma}(\mathbf{q}) \quad (\text{B1})$$

where σ denotes the polarization of ρ and

$$T_\sigma^{I=0}(E; p_1 p_2 p_3; \mathbf{q}) \equiv \langle p_1^+ p_2^- p_3^0 | T^{I=0}(E) | \rho(-\mathbf{q}) \pi(\mathbf{q}); \sigma \rangle \quad (\text{B2})$$

$$V_{\omega \rightarrow \rho\pi}^{\lambda\sigma}(\mathbf{q}) \equiv \langle \rho(-\mathbf{q}) \pi(\mathbf{q}); \sigma | V^{I=0} | \omega, \lambda \rangle \quad (\text{B3})$$

With straightforward calculation it can be shown that

$$T^\lambda(E; p_1, p_2, p_3) = A_{12}^\lambda(E) + A_{23}^\lambda(E) + A_{31}^\lambda(E)$$

where $A_{ij}^\lambda(E)$ is short for $A^\lambda(E; p_i, p_j)$ given by

$$A^\lambda(E; p, k) = \sqrt{\frac{1}{6}} \sum_\sigma \frac{1}{(2\pi)^3 2E_\rho(\mathbf{k})} V_{\rho \rightarrow \pi\pi}^\sigma(\mathbf{p}^*) \frac{W(E; \mathbf{k}) - m_\rho^B}{W(E; \mathbf{k}) - m_\rho^B - \Sigma(W(E; \mathbf{k}))} \frac{1}{E - E_\rho(\mathbf{k}) - E_\pi(\mathbf{k})} V_{\omega \rightarrow \rho\pi}^{\lambda\sigma}(\mathbf{k}) \quad (\text{B4})$$

where $\sqrt{\frac{1}{6}}$ is the isospin factor, $\Sigma = \Sigma_{\pi\pi} + \Sigma_{\omega\pi}$ defined in

Eq.(16,17), \mathbf{p}^* is the momentum \mathbf{p} boosted in ρ rest frame

since we have boosted the T-matrix element into ρ rest frame and $W(E; \mathbf{k}) \equiv \sqrt{(E - E_\pi(\mathbf{k}))^2 - \mathbf{k}^2}$. Therefore, the spin-averaged decay width is given by

$$\begin{aligned} \bar{\Gamma} &= \frac{(2\pi)^4}{(2\pi)^6 2m_\omega} \frac{1}{3} \sum_\lambda \int d\Phi_3 |T^\lambda(m_\omega; p_1, p_2, p_3)|^2 \quad (\text{B5}) \\ &= \frac{(2\pi)^4}{(2\pi)^6 2m_\omega} \int d\Phi_3 \sum_\lambda \left\{ |A_{23}^\lambda(m_\omega)|^2 + \right. \\ &\quad \left. 2 \operatorname{Re} (A_{23}^\lambda(m_\omega) A_{31}^{\lambda*}(m_\omega)) \right\} \quad (\text{B6}) \end{aligned}$$

where $d\Phi_3$ is the Lorentz-invariant three-body phase space element defined in [18]. It is convenient to take $d\Phi_3 \propto dm_{12} d\Omega_3 d\Omega_1^*$ and $\propto dm_{12}^2 dm_{23}^2 d\Omega_{\text{Euler}}$ for the integration of $|A|$ term and interference term, respectively. $V_{\rho \rightarrow \pi\pi}^\sigma$ and $V_{\omega \rightarrow \rho\pi}^{\lambda\sigma}$ can be written as two forms. The manifestly Lorentz-invariant one is convenient for the integration of THE interference term and the other

for THE $|A|^2$ term,

$$V_{\rho \rightarrow \pi\pi}^\sigma(\mathbf{k}) = -(2\pi)^3 \sqrt{2} g_{\rho\pi\pi} \epsilon_\mu(\mathbf{0}, \sigma) (k_1^* - k_2^*)^\mu u_{\pi\pi} \quad (\text{B7})$$

$$= (2\pi)^{\frac{9}{2}} \left(\sqrt{2E_\pi(\mathbf{k})} \right)^2 \sqrt{2m_\rho^B} Y_{1\sigma}(\hat{\mathbf{k}}) V_{\pi\pi}(\mathbf{k}) \quad (\text{B8})$$

$$\begin{aligned} V_{\omega \rightarrow \rho\pi}^{\lambda\sigma}(\mathbf{k}) &= (2\pi)^3 \sqrt{3} g_{\omega\rho\pi} \epsilon^{\mu\nu\alpha\beta} P_\mu \epsilon_\nu(\mathbf{0}, \lambda) P'_\alpha \epsilon_\beta^*(-\mathbf{k}, \sigma) \quad (\text{B9}) \\ &= -\sqrt{8\pi} (2\pi)^3 m_\omega g_{\omega\rho\pi} C_{11}(1\lambda; \lambda - \sigma\sigma) Y_{\lambda-\sigma}^1(\hat{\mathbf{k}}) |\mathbf{k}| \quad (\text{B10}) \end{aligned}$$

where ϵ is the polarization vector, $u_{\pi\pi}$ and $V_{\pi\pi}$ are the form factor and potential defined in Eq.(9) and Eq.(7), respectively. $p_{1/2}^*$ are the four-vectors of π , P and P' are the four-vectors of ω and ρ , respectively. We do not introduce a form factor for $V_{\omega \rightarrow \rho\pi}$ since there is no loop integral related to it. Following that in Ref.[70], the interference term is given by,

$$\begin{aligned} \sum_\lambda \operatorname{Re} (A_{23}^\lambda(m_\omega) A_{31}^{\lambda*}(m_\omega)) &= \frac{(2\pi)^6 g_{\rho\pi\pi}^2 g_{\omega\rho\pi}^2}{4E_\rho(\mathbf{p}_3) E_\rho(\mathbf{p}_1)} \frac{(m_{12} - m_\rho^B)(m_{23} - m_\rho^B)}{(m_\omega - E_\rho(\mathbf{p}_3) - E_\pi(\mathbf{p}_3))(m_\omega - E_\rho(\mathbf{p}_1) - E_\pi(\mathbf{p}_1))} u_{\pi\pi}(\mathbf{p}_1^*) u_{\pi\pi}(\mathbf{p}_1) \\ &\times \operatorname{Re} \left[\frac{1}{m_{12} - m_\rho^B - \Sigma(m_{12})} \left(\frac{1}{m_{23} - m_\rho^B - \Sigma(m_{23})} \right)^* \right] \begin{vmatrix} P^2 & P \cdot (p_2 + p_3) & P \cdot (p_3 - p_2) \\ P \cdot (p_1 + p_2) & (p_1 + p_2) \cdot (p_2 + p_3) & (p_1 + p_2) \cdot (p_3 - p_2) \\ P \cdot (p_2 - p_1) & (p_2 - p_1) \cdot (p_2 + p_3) & (p_2 - p_1) \cdot (p_3 - p_2) \end{vmatrix} \quad (\text{B11}) \end{aligned}$$

$|\mathbf{p}_1|, |\mathbf{p}_3|$ and the elements in the determinant can be easily expressed in terms of m_{12}^2 and m_{23}^2 . On the other

hand, the $|A^\lambda|^2$ term is given by

$$\begin{aligned} \int d\Omega_3 d\Omega_1^* \sum_\lambda |A_{23}^\lambda(m_\omega)|^2 &= \frac{m_\omega^2}{2} \left(\frac{1}{(2\pi)^3 2E_\rho(\mathbf{p}_3)} \right)^2 \left(\frac{1}{m_\omega - E_\rho(\mathbf{p}_3) - E_\pi(\mathbf{p}_3)} \right)^2 \left| \frac{W(m_\omega; \mathbf{p}_3) - m_\rho^B}{W(m_\omega; \mathbf{p}_3) - m_\rho^B - \Sigma(W(m_\omega; \mathbf{p}_3))} \right|^2 \\ &\times \left((2\pi)^3 2\sqrt{2} g_{\rho\pi\pi} |\mathbf{p}_1^*| u_{\pi\pi}(|\mathbf{p}_1^*|) \right)^2 \left((2\pi)^3 \sqrt{8\pi} m_\omega g_{\omega\rho\pi} |\mathbf{p}_3| \right)^2 \quad (\text{B12}) \end{aligned}$$

With these ingredients $\Gamma_{\omega \rightarrow \rho\pi \rightarrow 3\pi}$ can then be calculated.

In Sec.(III C) we found that when $V_{\omega\pi} = 0$, $g_{\rho\pi\pi}$ and $\Lambda_{\rho\pi\pi}$ can be fixed at 7.07 and 890 MeV, respectively. It is expected that the introduction of the $\omega\rho\pi$ vertex would slightly shift these parameters, we try to take $g_{\rho\pi\pi}$ and $\Lambda_{\rho\pi\pi}$ at 7.40 and 900 MeV, respectively. Besides, we assume that $\Lambda_{\omega\rho\pi} = \Lambda_{\rho\pi\pi}$. The remaining two parameters m_ρ^B and $g_{\omega\rho\pi}$ are constrained by $\Gamma_{\omega \rightarrow 3\pi}$ and $\delta_{\pi\pi \rightarrow \pi\pi}^{\ell=1}$.

If we adopt $g_{\omega\rho\pi} = 18/\text{GeV}$, which is close to that in Ref.[51], and $m_\rho^B = 870$ MeV, it is found that

$$\Gamma_{\omega \rightarrow \rho\pi \rightarrow 3\pi} = 7.12 \text{ MeV} \quad (\text{B13})$$

while the experimental value of the partial decay width $\Gamma_{\omega \rightarrow 3\pi}^{\text{ex}} = 7.74(13) \text{ MeV}$. The 10% discrepancy is accounted for by the neglected direct interaction between the $|\omega\rangle$ and the $|3\pi\rangle$ channel[70]. Furthermore, the

phase shift defined by Eq.(19) can also be obtained and shown in Fig.8 The approximate consistence between the theoretical and experimental results justify the values adopted. Furthermore, it is interesting that the extrapolated m_ρ^B of HSC, MILC and Bulava *et al.* in scheme C are nearly the same as that adopted here.

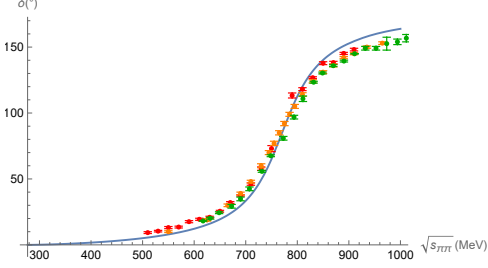


FIG. 8. Phase shift calculation by Eq.(19) using parameters $g_{\omega\rho\pi} = 18/\text{GeV}$, $\Lambda_{\omega\rho\pi} = \Lambda_{\rho\pi\pi} = 900 \text{ MeV}$, $g_{\rho\pi\pi} = 7.40$ and $m_\rho^B = 870 \text{ MeV}$ at the physical pion mass μ_π . The points in the figure are experimental values from Refs. [71–73].

Appendix C: Table of $C_{\Gamma,G}$

In this appendix the values of $C_{\Gamma,G}$ are given. As in the main context, $C_{\Gamma,G}$ is the reduction coefficient. To be more specific, the non-zero space spanned by $|\alpha; e_n, M\rangle$ furnish a representation labelled by Γ_∞ which is irreducible for G_∞ but generally reducible for subgroup G ,

i.e., a restricted representation for G . Therefore, with $C_{\Gamma,G}$, the Γ_∞ can be decompose into the direct sum of the irreducible representation of G . Furthermore, thanks to the Wigner-Eckart theorem, it is sufficient to take $a = 1$ without loss of generality. The non-vanishing $[C_{\Gamma,G}]_{M,a=1}$ relevant to the present work is given in the Table.(VI). For more general result one can refer to, for example, Ref. [47, 48].

(Γ, G)	$\sum_M [C_{\Gamma,G}]_{M,a=1} M\rangle$
(T_1, O_h)	$\frac{1}{\sqrt{2}} 1\rangle - \frac{1}{\sqrt{2}} -1\rangle$
(A_1, C_{4v})	$ 0\rangle$
(E, C_{4v})	$ -1\rangle$
(A_1, C_{3v})	$ 0\rangle$
(E, C_{3v})	$ -1\rangle$
(A_1, C_{2v})	$ 0\rangle$
(B_1, C_{2v})	$\frac{1}{\sqrt{2}} -1\rangle + \frac{1}{\sqrt{2}} 1\rangle$
(B_2, C_{2v})	$\frac{1}{\sqrt{2}} -1\rangle - \frac{1}{\sqrt{2}} 1\rangle$

TABLE VI. Values of $[C_{\Gamma,G}]_{M,a=1}$ relevant to the present work. $|M\rangle$ is short for the state $|\alpha; e_n, M\rangle$ defined in Eq.(24) with $J = 1$.

Appendix D: HEFT fits to lattice QCD spectra

Here, we show all the other fit results for the various lattice QCD data sets collected besides that given in Fig. 1.

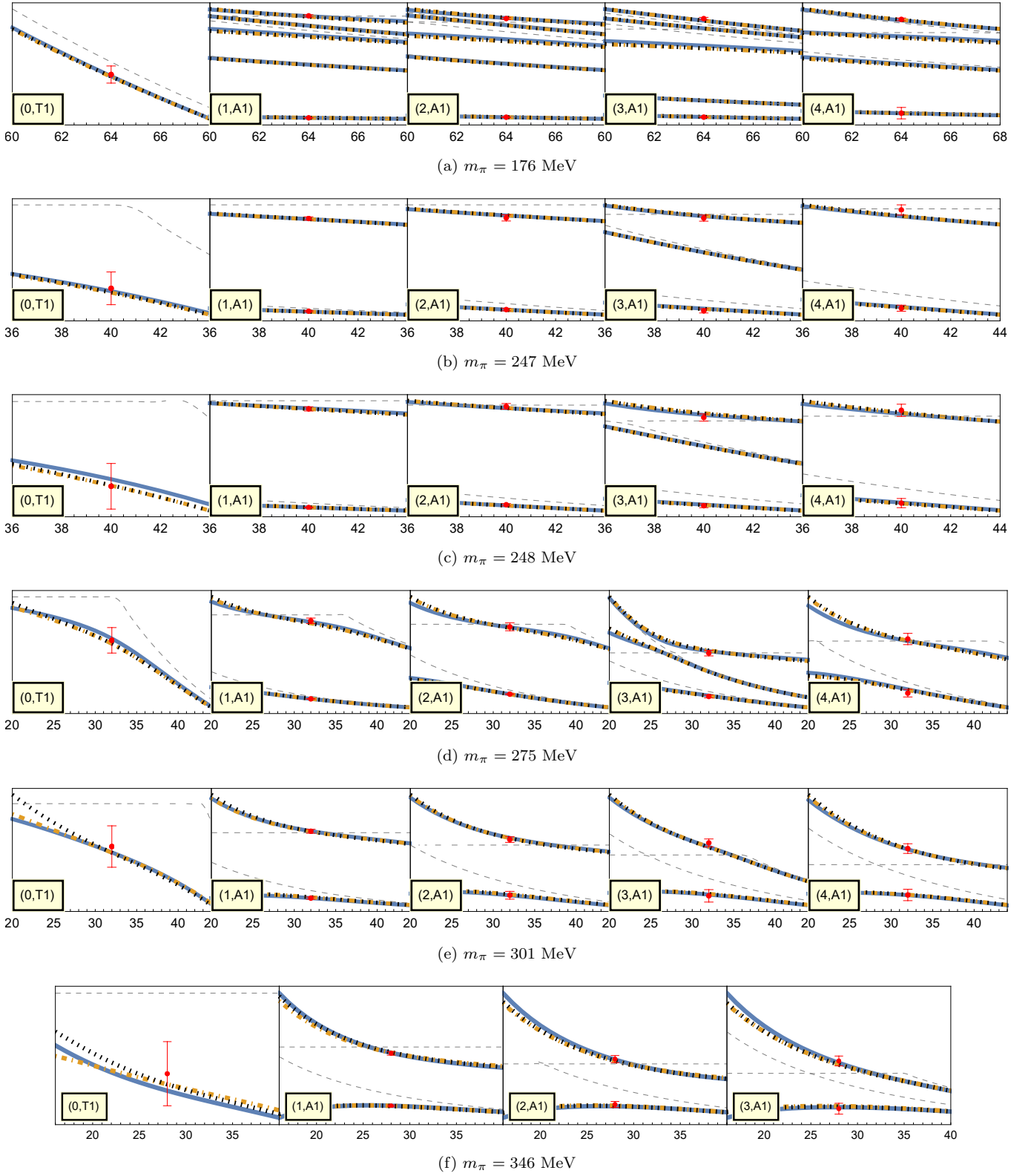


FIG. 9. Same as in Fig. 1 but for the MILC collaboration [33].

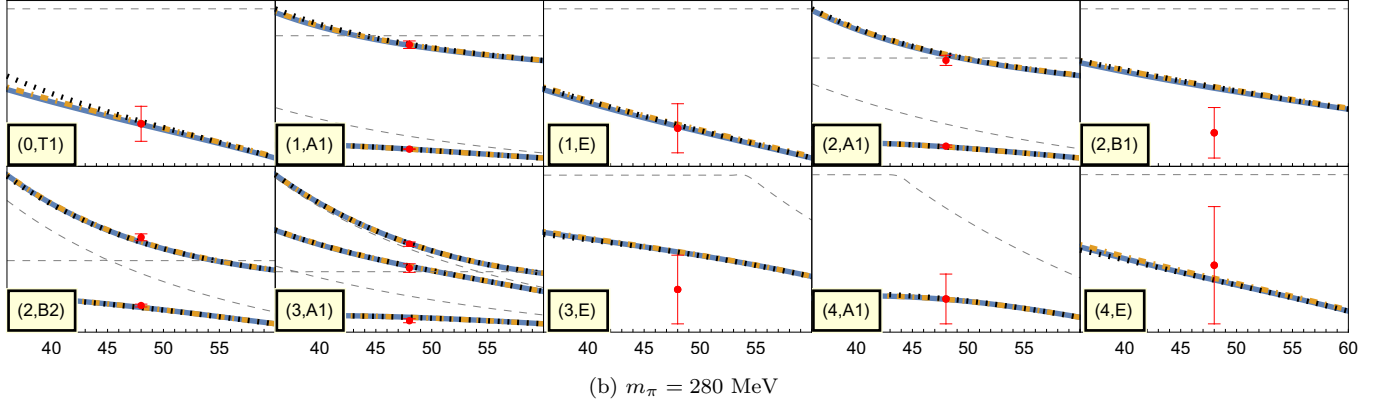
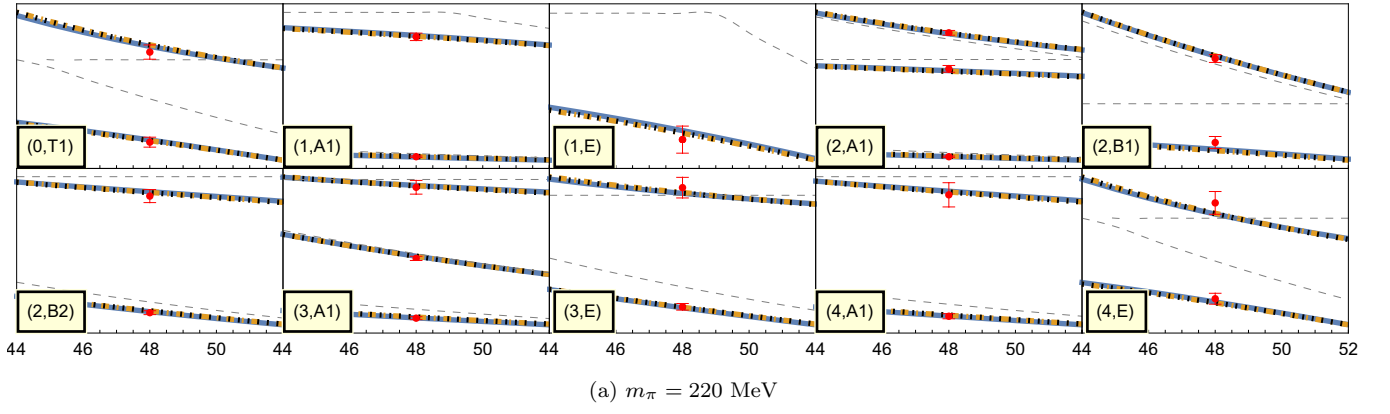


FIG. 10. Same as in Fig. 1 but for other m_π by Bulava *et al.* [34].

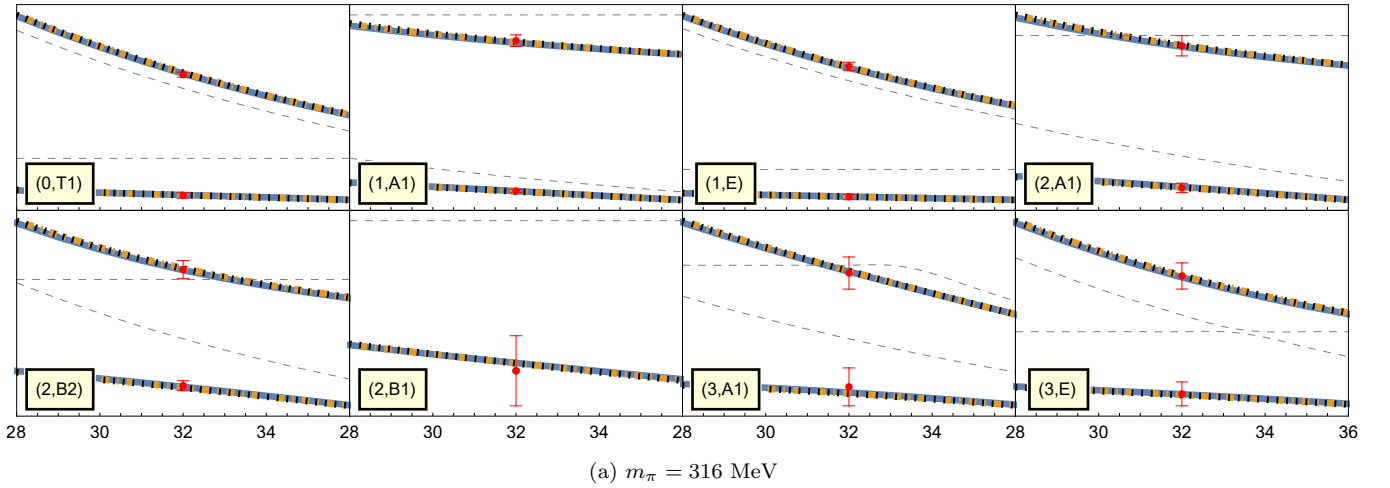


FIG. 11. Same as in Fig. 1 but for C. Alexandru *et al.* [29]

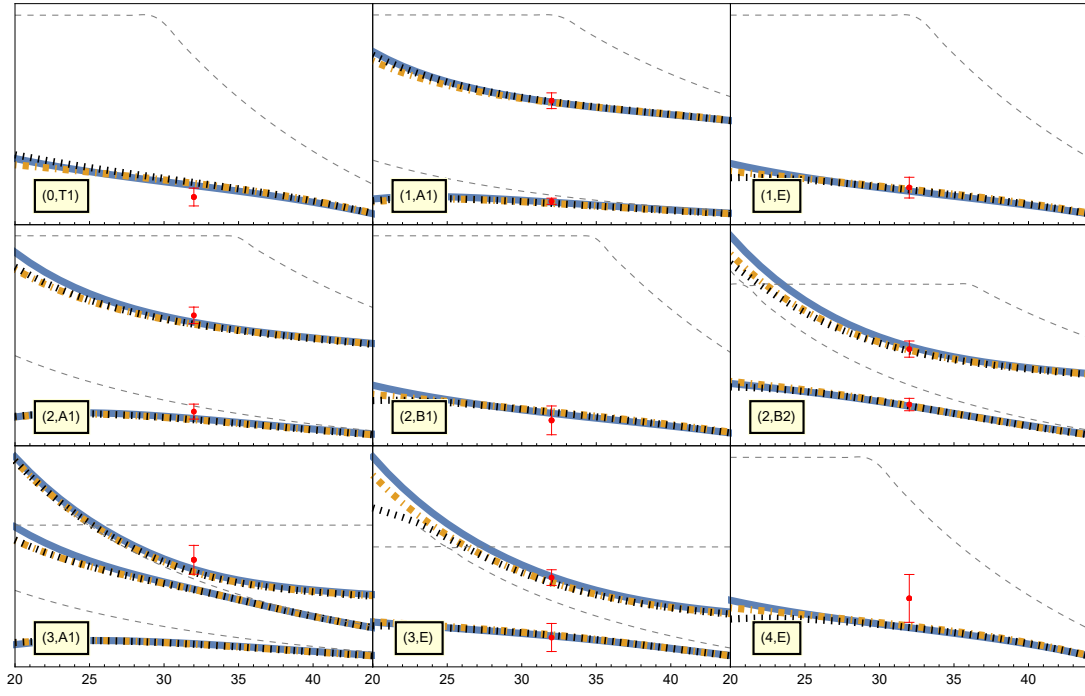
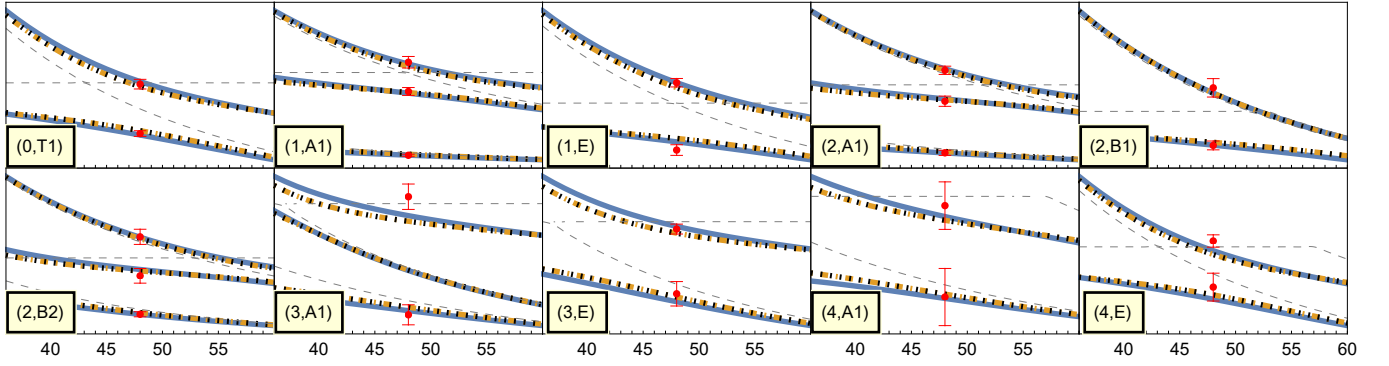
(a) $m_\pi = 262$ MeV(b) $m_\pi = 302$ MeV

FIG. 12. Same as in Fig. 1 but for the ETMC collaboration [28].

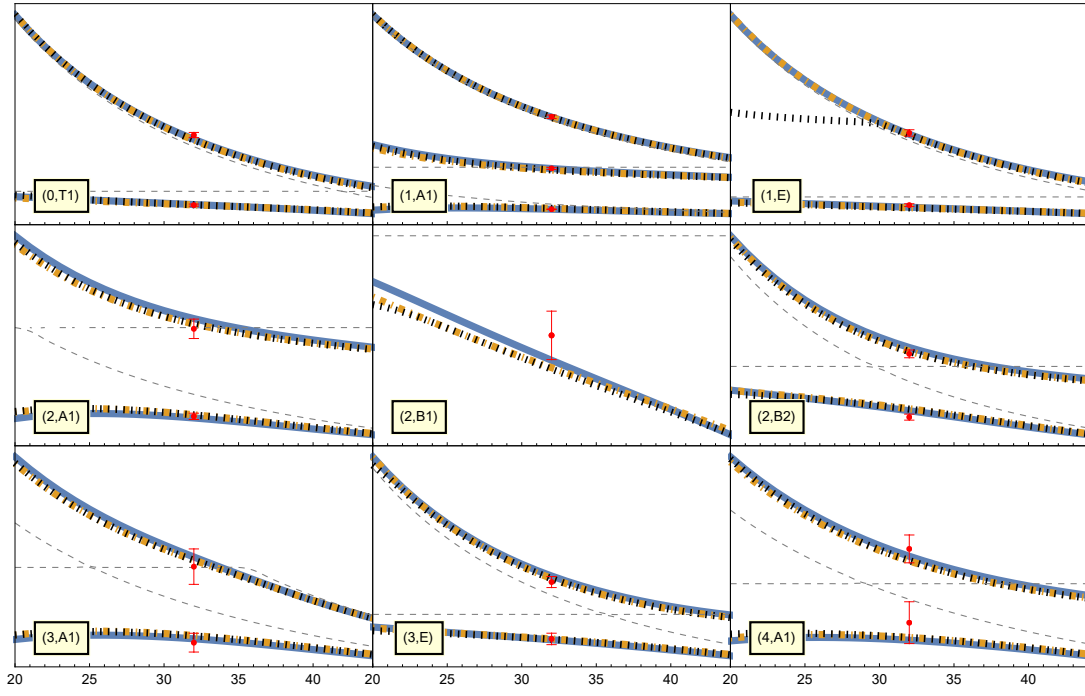
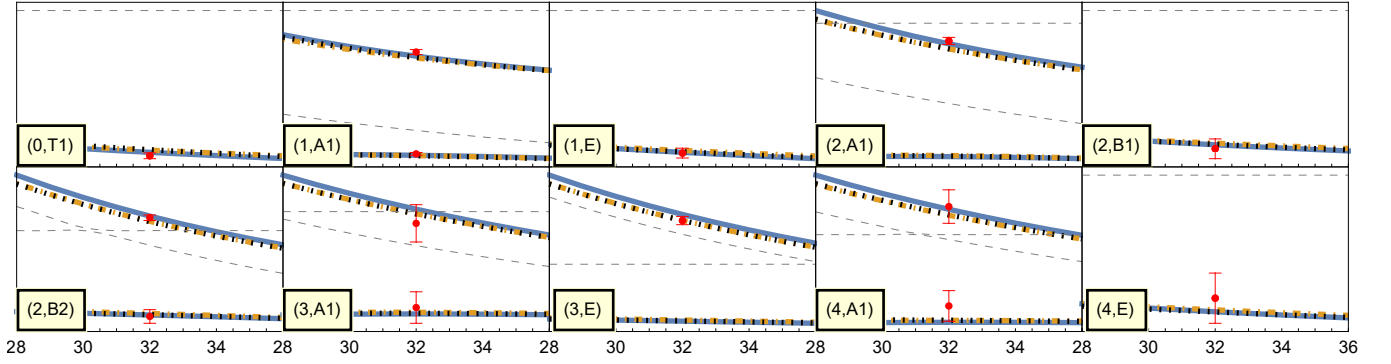
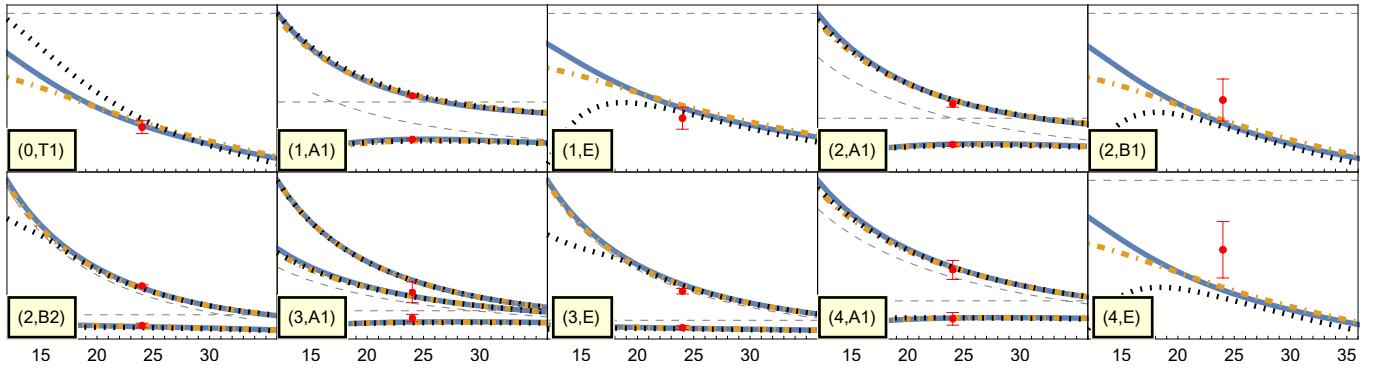
(a) $m_\pi = 322$ MeV(b) $m_\pi = 376$ MeV(c) $m_\pi = 386$ MeV

FIG. 13. Same as in Fig. 1 but for the ETMC collaboration [28]. The turning point of the black dotted line for $m_\pi = 322$ MeV is due to an avoided level crossing when the $\omega\pi$ channel is included.

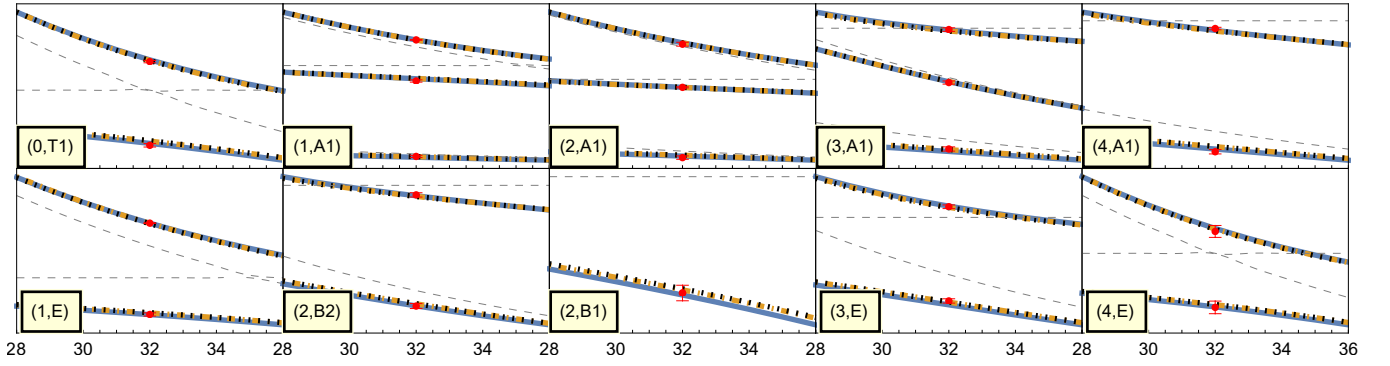
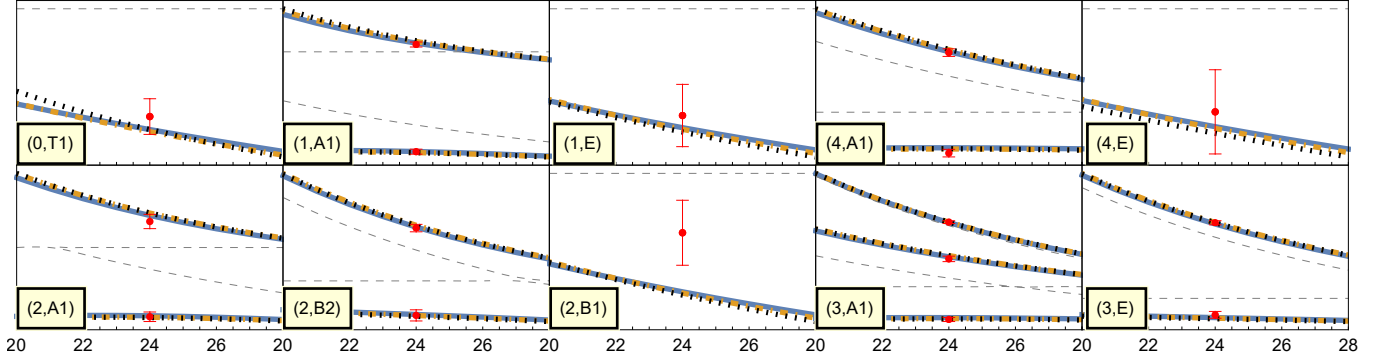
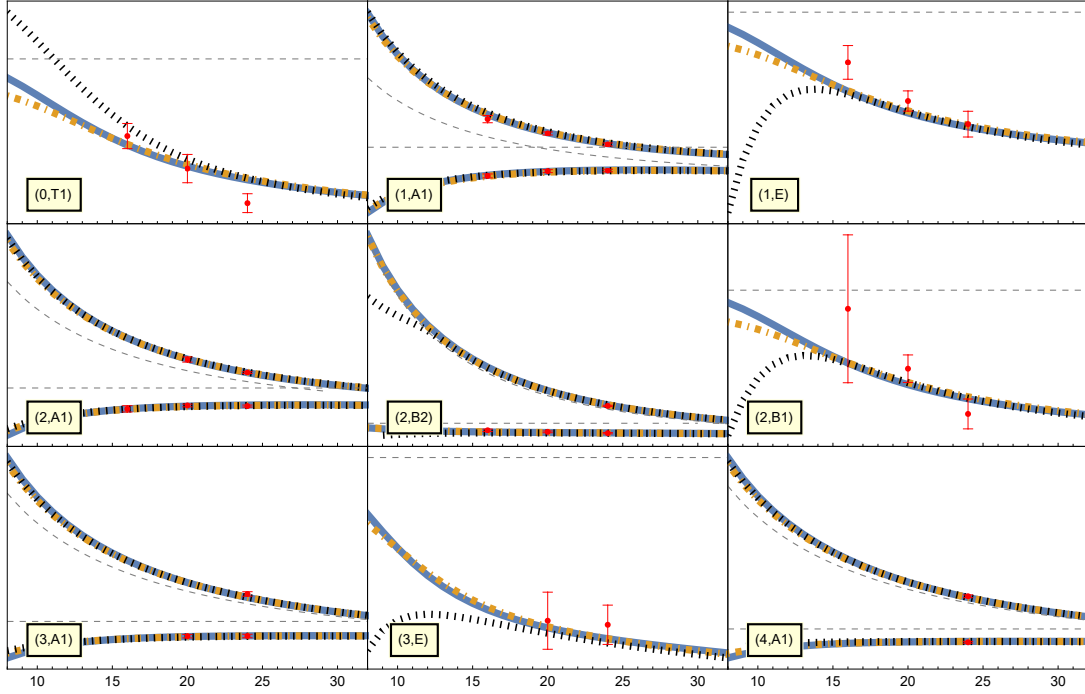
(a) $m_\pi = 236$ MeV(b) $m_\pi = 330$ MeV(c) $m_\pi = 391$ MeV

FIG. 14. Same as in Fig. 1 but for the HSC collaboration [26, 27, 36].

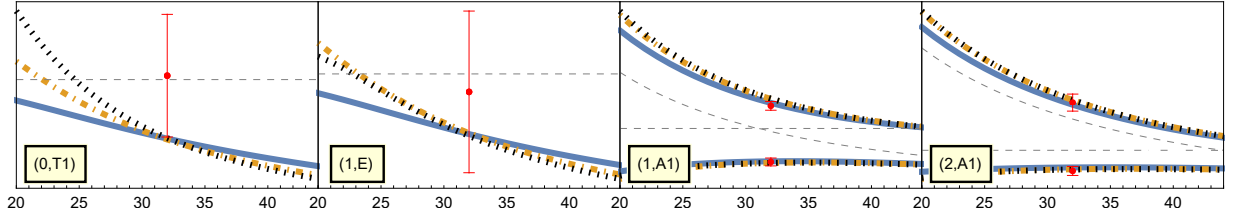


FIG. 15. Same as in Fig. 1 but for the PACS-CS collaboration [74].

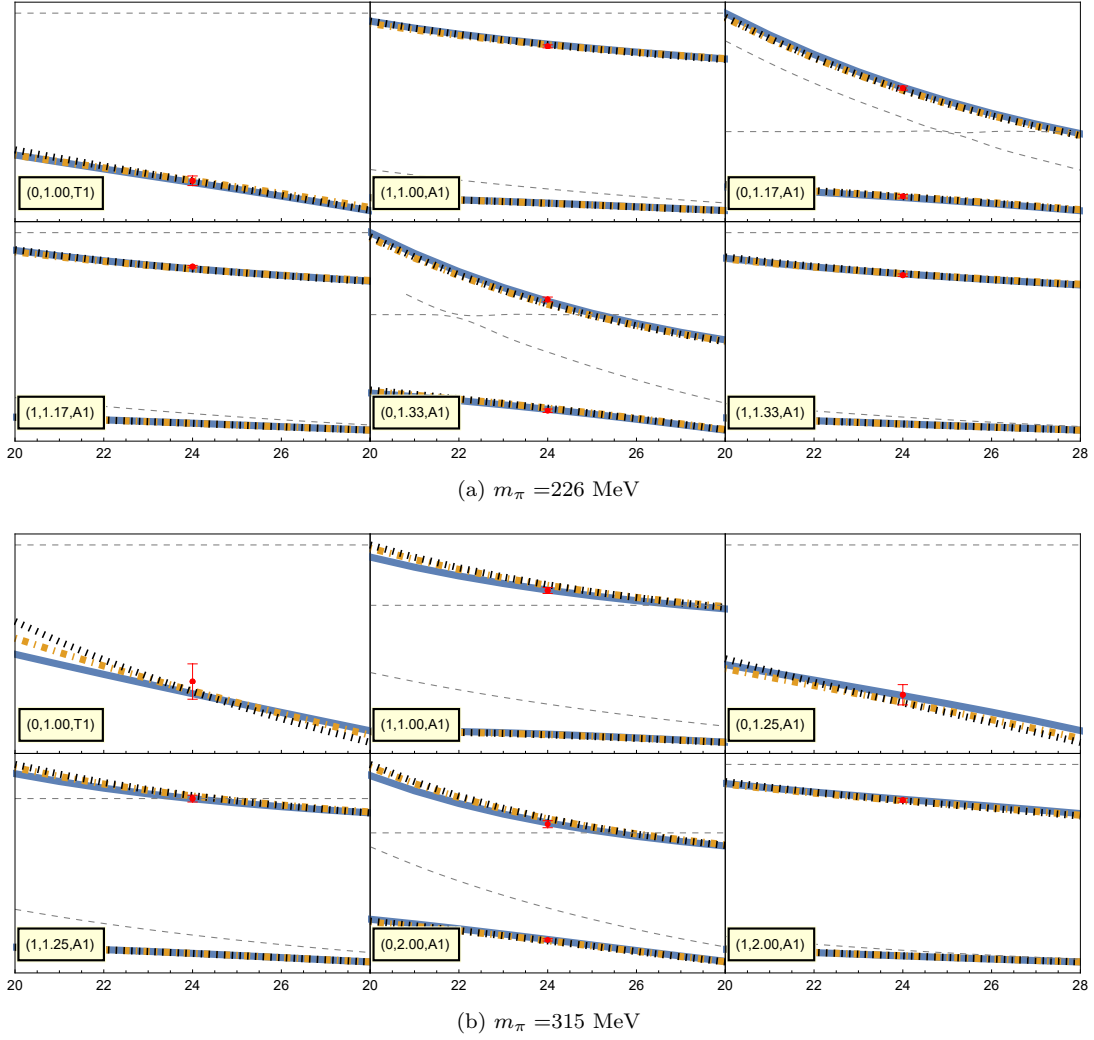


FIG. 16. Same as in Fig. 1 but for Guo *et al.* [32]. Note that there is an additional quantity η denoting the elongation factor in the yellow box compared to the others.